

**Keywords:** convection initiation, Doppler lidar, Doppler radar, cloud seeding

## **The new Mountain Observatory of the Project “Optimizing Cloud Seeding by Advanced Remote Sensing and Land Cover Modification (OCAL)” in the United Arab Emirates: First results on Convection Initiation**

### **Authors:**

**Oliver Branch<sup>1</sup>, Andreas Behrendt<sup>1</sup>, Osama Alnayef<sup>1</sup>, Florian Späth<sup>1</sup>, Thomas Schwitalla<sup>1</sup>, Marouane Temimi<sup>2</sup>, Michael Weston<sup>3</sup>, Sufian Farrah<sup>4</sup>, Omar Al Yazeedi<sup>4</sup>, Siddharth Tampi<sup>4</sup>, Karel de Waal<sup>4</sup>, Volker Wulfmeyer<sup>1</sup>**

### **Affiliation:**

<sup>1</sup>Institute of Physics and Meteorology, University of Hohenheim, 70593 Stuttgart, Germany.

<sup>2</sup>Department of Civil, Environmental, and Ocean Engineering (CEOE), Stevens Institute of Technology, New Jersey, USA

<sup>3</sup>Khalifa University of Science and Technology, Abu Dhabi, United Arab Emirates.

<sup>4</sup>National Center for Meteorology, Abu Dhabi, United Arab Emirates.

Corresponding author: Oliver Branch (oliver\_branch@uni-hohenheim.de)

### **Key points:**

- Advanced remote sensing synergies are essential for the understanding of convection initiation and the forecasting of seedable clouds.
- Scanning Doppler lidar and cloud radar facilitate observation of clear air dynamics and the subsequent evolution of convective cells.
- During two cases, the decisive role of low level orographic wind flow distortion and convergence is exemplified and quantified.

### **Abstract**

In this study, we discuss a new mountain peak observatory in the United Arab Emirates (UAE). Using coordinated scan patterns, a Doppler lidar and cloud radar were employed to study seedable convective clouds, and identify pre-convection initiation (CI) clear-air signatures. The instruments were employed for approximately two years in an extreme environment with a high vantage point for observing valley wind flows and convective cells. The instruments were configured to run synchronized polar (PPI) scans at 0°, 5°, and 45° elevation angles and vertical cross-section (RHI) scans at 0°, 30°, 60, 90°, 120°, and 150° azimuth angles. Using this output imagery, along with local C-band radar and satellite data, we were able to identify and analyze several convective cases. To illustrate our results, we selected two cases in unstable conditions - the 5 and 6 September 2018. In both cases, we

observed areas of convergence/divergence, particularly associated with wind flow around a peak 2 km to the south-west. The extension of these deformations were visible in the atmosphere as high as 3 km above sea level. Subsequently, we observed convective cells developing in the same directions – apparently connected with these phenomena. The cloud radar images provided detailed observations of cloud structure, evolution, and precipitation. In both convective cases, pre-convective signatures were apparent before CI, in the form of convergence, wind shear structures, and updrafts. These results demonstrate the value of synergetic observations for understanding convection initiation, improvement of forecast models, and cloud seeding guidance.

## 1. Introduction

Here we present a unique synergy of scanning Doppler lidar and cloud radar on a peak of the Al Hajar Mountains in the United Arab Emirates (UAE). The purpose of this unique observatory is to study the clear-air pre-convective environment, convergence lines, and subsequent convection initiation (CI).

The UAE is one of the Arabian Peninsula's driest countries with an annual precipitation amount varying from 20-40 mm up to 140-150 mm per year (Almazroui, 2012; Sherif et al., 2014). Furthermore, the whole region is projected to be extremely vulnerable to climate change (Pal and Eltahir, 2016) and UAE precipitation is projected to decrease by 20% by the year 2050 and 45% by 2100, compared to the period 1961 to 1990 (Odhiambo, 2017). In order to counteract this water scarcity, the 'UAE Research Program for Rain Enhancement Science' ([UAEREP](http://www.uaerep.ae), see <http://www.uaerep.ae>) was initiated to intensify scientific research into deliberate weather modification. This program focuses primarily on cloud seeding approaches and operational hygroscopic seeding has been ongoing for some time in the UAE. However, much research remains to reduce the uncertainty of convective cloud seeding efficacy, especially relating to the detection of positive impacts within acceptable attribution error limits (e.g. see Breed et al., 2007; Bruintjes, 1999).

Other rain enhancements approaches are also now being considered, particularly weather modification through deliberate land-surface change (see Becker et al., 2013; Branch et al., 2014; Branch and Wulfmeyer, 2019; Wulfmeyer et al., 2014) and such methods may be more efficient and reliable than cloud seeding. In that context, the University of Hohenheim proposed the project 'Optimizing Cloud Seeding by Advanced Remote Sensing and Land Cover Modification' ([OCAL](#)) and was funded by UAEREP for a duration of three years 2016-2019.

In this context, the OCAL sub-project had the following aims:

1. To provide the UAE with unique modeling and observational capabilities for improving cloud process understanding, forecasting, and cloud seeding guidance
2. To study the effect of land surface modifications on the initiation and amplification of convective precipitation over the UAE

This particular study primarily addresses the first aim and is based on the following objectives:

- O1: Improve understanding and forecasting of convergence zones and CI in the UAE
- O2: Provide the UAE with the knowledge towards an operational forecast system optimized for high-resolution cloud and precipitation forecasts

These objectives are based on the following two hypotheses:

- H1: Better understanding and modeling of the pre-convective environment and CI is a pre-requisite for an improved simulation of clouds and precipitation
- H2: For reliable guidance on cloud seeding an NWP-based nowcasting system is necessary including the assimilation of clear-air remote sensing data

H1 is based on the fact that current model systems still have severe deficiencies simulating the pre-convective environment leading to the formation of clouds (e.g. Heinze et al., 2017; Macke et al., 2017; Nelli et al., 2020a). Good simulations of dynamics and thermodynamics are prerequisites for accurate cloud modeling. This requires both advanced clear-air and cloud observations and the development of model systems operating down to the turbulence-permitting scale (e.g. see Bauer et al., 2020).

H2 states that the best means of incorporating clear-air, cloud, and precipitation measurements within model simulations is data assimilation (e.g. Pu et al., 2010; Schwitalla and Wulfmeyer, 2014; Thundathil et al., 2020) which leads to an optimal analysis of meteorological conditions. In contrast, cloud seeding guidance from nowcasting, based on existing remote sensing data alone, e.g., satellite radiances and radar, suffers from erroneous results, with little lead time for initiating cloud seeding operations. This is mainly due to missing information concerning the clear-air thermodynamic environment, e.g., upper level inversions as well as inflows and outflows of moisture. A NWP-based nowcasting system can provide optimized performance with respect to the simulation of clouds for process understanding and cloud seeding guidance.

Two other studies were conducted within the OCAL project to address objectives O1 and O2. The first study provides context for regional orographic convection initiation. In this study, we generated statistics of summer CI events between 2010 and 2016 for the Al Hajar Mountains by identifying CI from satellite brightness temperatures, using regionally-prescribed thresholds (Branch et al., 2020). The second study provided a step toward a cloud seeding forecast system, using a convection-permitting (CP) model ensemble approach, evaluated with surface meteorological and remote sensing data (Schwitalla et al., 2020). In these works, insight was gained into the necessary pre-convective environment for CI, via measured and simulated indices such as convective available potential energy (CAPE). These insights have been extremely valuable, complementing several other regional forecasting and verification studies (Chaouch et al., 2017; Fonseca et al., 2020; Francis et al., 2020; Valappil

et al., 2020; Wehbe et al., 2019), and observational and process studies (Karagulian et al., 2019; Nelli et al., 2020a, 2020b; Weston et al., 2019).

To further address objective O1 and hypothesis H1, a key component of our research was the realization of new measurements of the pre-convective environment and convection CI. There have been several observational and modelling studies on convective process employing instrumentation synergies (e.g. Aoshima et al., 2008; Bauer et al., 2015; Behrendt et al., 2011; Groenemeijer et al., 2009; Schmitalla et al., 2020; Smith et al., 2014; Wulfmeyer et al., 2011). However, to our knowledge a synergy of clear-air and cloud measurements has not been attempted before in this region.

To address this omission, we employed a scanning Doppler lidar (DL) and Doppler cloud radar (DCR), to be operated at a site where convection initiation and precipitation development are likely during the campaign. The DL allows us to observe clear-air dynamics, given the presence of sufficient aerosols, and the Doppler cloud radar enables us to study larger cloud hydrometeors as well as cloud dynamics. Both instruments were configured with synchronized alternating polar plane indicator (PPI) and range height indicator (RHI) modes scan patterns. The observations should provide deep insights into convective processes in the Al Hajar Mountains and identify the necessary pre-convective conditions for seedable clouds.

We demonstrate the value of the observatory with two convective case studies using the DL and DCR observations, complemented by data from precipitation radar, geostationary satellites, radiosondes, and analysis/reanalysis model simulations from the European Centre for Medium-Range Weather Forecast (ECMWF). These data provide context in respect to synoptic atmospheric conditions, and comparisons with our observations in respect to clouds and precipitation.

The structure of this work is as follows. In Section 2 ‘Materials and Methods’, we describe the study area and its characteristics; we discuss the rationale behind the selection of our measurement observatory; we provide detail of the instruments and corresponding measurements; and describe the other datasets used for the study. In Section 3 ‘Results and Discussion’ we introduce the two convective case studies used to illustrate our observations and present our findings. Finally, in Section 4 ‘Summary’ we discuss the implications of our study.

## **2. Materials, methods, and logistical preparations**

Our approach for executing the OCAL observatory campaign was as follows:

1. Conduct an investigation into regional climate particularly with respect to precipitation and clouds over the UAE.
2. Design optimal observatory configuration, including the selection of suitable instruments and configuration for remote operation and data collection.

3. Select optimal mountain site based on climatological/logistical constraints.
4. Conduct observational campaign for 1-2 years.
5. Analysis of DL and DCR observations during case studies, alongside several other remote sensing and model datasets

Steps 1-4 are now presented in the following sections. The analysis in Step 5 is presented in Section 4 (Results).

## **2.1. Geography and climate of the study region**

### **2.1.1. UAE and surrounding regional climate**

The climate over the north-east Arabian Peninsula, where the UAE is located, is controlled generally by four weather systems: a) troughs which originate from the Atlantic and Mediterranean Sea in winter, b) the summer monsoon, c) cyclones from the Arabian Sea during June and October, and d) locally forced convective storms over the Al Hajar Mountains in summer (Branch et al., 2020; Brintjes and Yates, 2003; Steinhoff et al., 2018). The UAE climate is characterized predominantly by high temperatures and very scarce precipitation. However, there are annual cycles, with the maximum precipitation and minimum temperatures occurring in winter, and the reverse in summer. Annual precipitation in the UAE ranges between 20-40 mm in the drier west to 130-140 mm in the higher Al Hajar Mountains of the east, mainly produced in the winter-spring time period according to Sherif et al. (2014). It should be noted however that rainfall in the region is difficult to measure, and to quantify with any certainty from existing rainfall data, between which there is considerable variability (Wehbe et al., 2019). In terms of cloud cover, clouds tend to occur more often over the Arabian Gulf during winter, whilst in the summer they are more prevalent over the Al Hajar Mountains (Kumar and Suzuki, 2019). In fact, there is a distinct west-east cloudiness trend, with more clouds occurring in the east close to the Al Hajar Mountains (the cities of Al Ain and Fujairah) than further west (Abu Dhabi and Sharjah) (Yousef et al., 2019). Despite this trend, during the summer (June to August [JJA]) in the Al Hajar region, subtropical subsidence inhibits summer precipitation to the extent that it represents only around 20% of the annual amount. And yet, summer in the Al Hajar Mountains may still likely to present the most potential for rainfall enhancement, given the more frequent occurrence of cumulus clouds during this season (Kumar and Suzuki, 2019; Yousef et al., 2019). For these reasons, the study area, and the observatory would be located within the Al Hajar Mountains, and a general focus would be on summertime periods. In the UAE the meteorological summer extends from June-September.

### **2.1.2. Al Hajar Mountain range**

The Al Hajar Mountains extend for approximately 400 km between 22.5°N and 26.4°N latitude, and between 55.8°E and 59.7°E longitude in the eastern UAE/northern Oman (see Figure 1a). The range runs parallel to the north-eastern coast of the Arabian Peninsula, with

the highest point reaching 3009 meters in Oman (Jebel Shams). There are distinct geophysical zones on each side of the mountains with coastal plains on the east side and desert and gravel plains to the west. Vegetation on the mountains is sparse, but some scrublands and woodlands do exist at lower elevations, and fruit trees are grown in the cooler valleys (Branch et al., 2020; Chambers et al., 2016). Generally, irrigation is needed to maintain vegetation on a permanent basis.

From June to September, weather conditions are often complex in the mountains, with summer convection being initiated by complex phenomena acting in concert. Upper-level disturbances from the southern monsoon flows can transport moisture towards the Arabian Peninsula and the UAE, especially when the position of the oscillating Inter Tropical Convergence Zone (ITCZ) is favorable (Böer, 1997; Brintjes and Yates, 2003; Schwitalla et al., 2020). There are also daytime sea breezes from both the Gulf of Arabia to the north, and the Gulf of Oman to the east, which can penetrate up to 50 km inland (Eager et al., 2008). At night, as the land-sea temperature gradients reverse, land breezes then develop which may interact with the southerly low-level nocturnal jet extending up from further south in Oman (Ranjha et al., 2015). The properties of this nocturnal jet may influence the strength and nature of the sea breeze on the following day (Schwitalla et al., 2020). Due to high sensible heat fluxes over land and the low-level wind shear induced by the sea breeze and low-level jet, boundary-layer convective motion often self-organizes into horizontal convective rolls (Schwitalla et al., 2020), with a structure thought to be determined by the ratio of the boundary-layer height and the Monin–Obukhov length (Weckwerth et al., 1997). These phenomena interact in such a way that the sea breeze advects moisture from the sea and the convective rolls transport the moisture vertically upwards. These local circulations are complicated further by the heterogeneity of the terrain and landscapes on either side of the mountains which lead to differential heating. These flows combine to initiate sporadic convective storms particularly in summer (e.g. Branch et al., 2020), and these can be intense enough to cause flash floods and erosion (Chowdhury et al., 2016; Wehbe et al., 2019). Sporadic flashfloods provide a much need resources, with large quantities of water being collected with dams for agricultural and residential use.

As part of our regional climate assessment, for the first time in the eastern UAE we generated multi-year statistics of summer CI events from 2010 to 2016 (see Branch et al., 2020) based on Meteosat (MFG) radiances (see Figure 1). The relatively few detectable CI events (387) occurring over the seven years reflects the aridity of the region. However, the available pixel resolution for the MFG longwave radiances was only around 5 km, which means that smaller convective cells may not have been detected and only the most substantial CI events were captured. It is possible that other deep convective clouds with a more limited horizontal scale occurred somewhat more often, and these smaller cells may in fact provide the best opportunity for rainfall enhancement. However, we can still see that larger-scale deep convective events do tend to initiate more toward the west of the mountains.

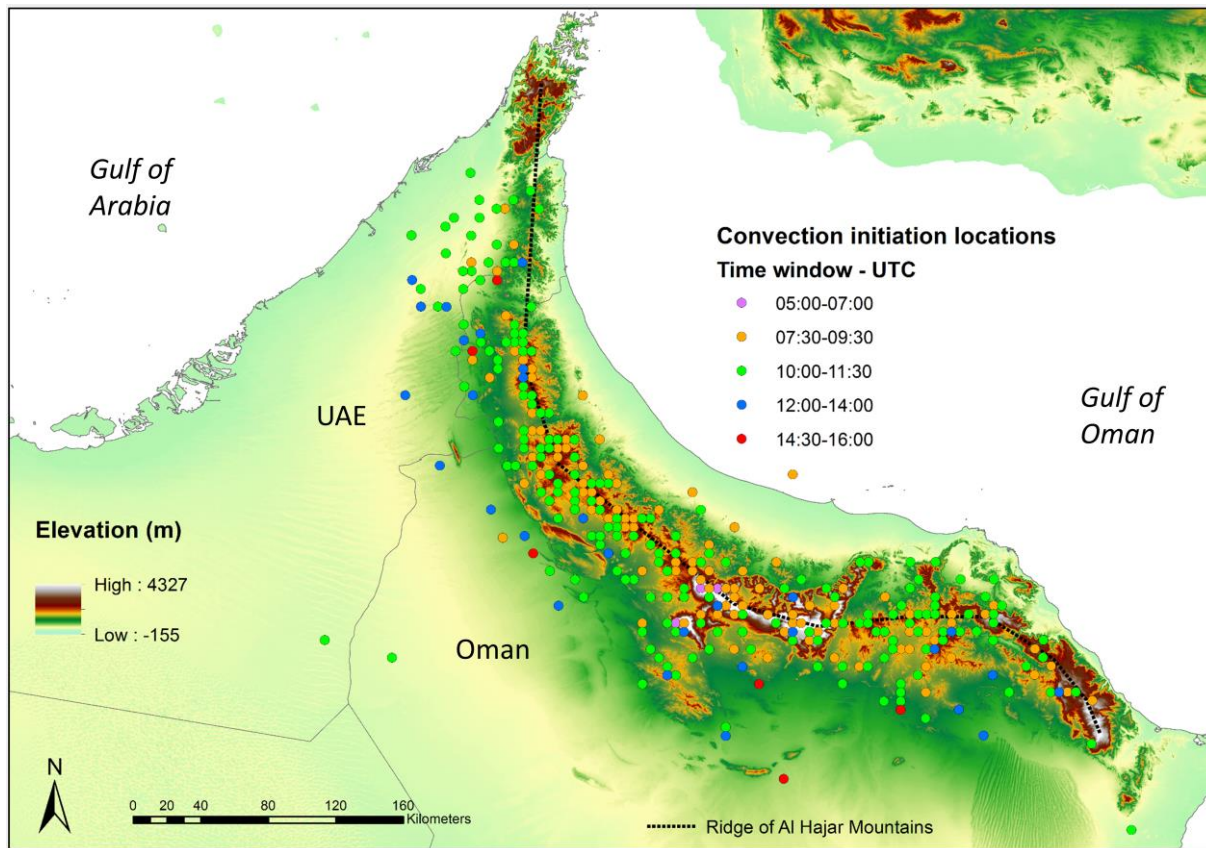


**Figure 1: Study area – The Al Hajar Mountains in the eastern UAE/northern Oman, showing elevation [m.a.s.l.] and a line marking the highest ridge through the mountains. Also marked on the map are summer CI events (2010-2016) as derived by Branch et al. (2020) from a Meteosat 8 infrared channel data using a back-tracing method. The times of CI occurrence are also indicated as dot colors. 387 events were detected.**

## 2.2. Selection of instrumentation

The following combination of instruments was chosen to study CI in the mountain range:

- a passive microwave radiometer (Radiometer Physics Gesellschaft mit beschränkter Haftung (RPG)-Humidity And Temperature PROfile (HATPRO), RPG-HATPRO) described by Temimi et al. (2020). Unfortunately, this data was not available during the analysis undertaken in this study.
- An AWS meteorological station was also generously added (later in our campaign) by the UAE's National Center for Meteorology (Al Farfar available at <https://www.ncm.ae>). The station measures standard variables such as temperature, humidity, pressure, wind speed, and wind direction. The station also contained a sky camera for visual inspection of weather conditions.

To order to observe the wind, aerosol particle, and cloud fields from the top of the OCAL observatory at Al Farfar, two remote sensing instruments from the Institute of Physics and Meteorology (IPM) at the University of Hohenheim were deployed:



- a HALO Streamline XR scanning Doppler lidar from Halo Photonics to measure the wind and aerosol fields in clear air.
- a MIRA-35 Ka-band scanning polarization Doppler cloud radar to measure cloud wind, reflectivity, and depolarization.

Analysis of observations from these last two instruments are the main focus of this work. A schematic of the intended scan patterns and scan ranges (as given by the manufacturer) are shown in Figure 2. The instrument scan patterns were synchronized and set to operate in a continuous pattern with a full sequence lasting one hour. The sequence included 360° rotating scans (plane-position indicators or PPIs) at elevation angles of ~0° and 45°, and six 180° vertical sweeps starting at 0°, 30°, 60°, 90°, 120°, and 150° azimuth angles (range-height indicators or RHIs). This sequence was designed to best capture low and mid-level perspectives of dynamics, cell evolution, and clouds simultaneously. A more detailed look at the programmed scan patterns and instrument specifications are shown in the following descriptions.

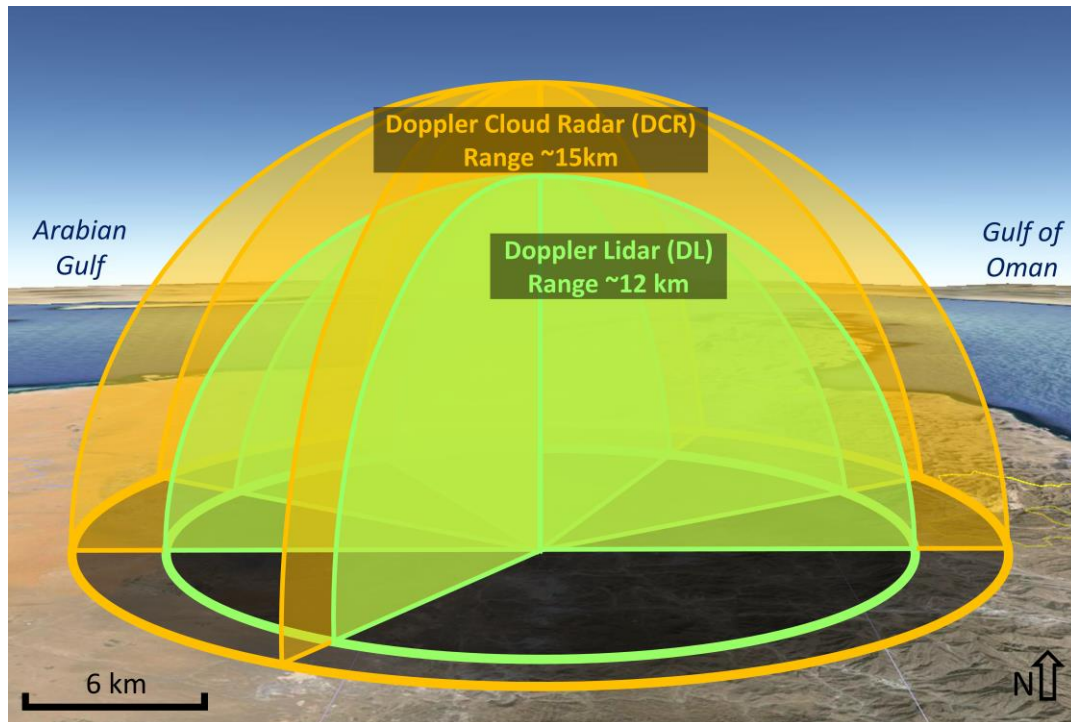


**Figure 2: Schematic of the DL and DCR range and plane-position indicator (PPI) and range-height indicator (RHI) scan patterns to generate polar and vertical cross-section images. In reality, more scans patterns are programmed than seen here. In green, the maximum range of the DL is shown, and in orange, that of the DCR. Background imagery taken from Google Earth Pro (2019).**

### 2.2.1. Doppler lidar (DL)

The Streamline XR Doppler lidar system from Halo Photonics allows a specified extended measurement range up to ~12 km (manufacturer specifications). It uses a wavelength of 1.5  $\mu\text{m}$  and a pulse repetition rate of 10 kHz. The DL uses aerosols and small particles in the



free atmosphere as wind tracers and can also provide data from inside of thin clouds. The lidar has a freely movable scanner head to point the laser beam in all directions. The measured wind velocity vector is orientated along the laser beam, known as line-of-sight wind velocity (hereafter, referred to simply as wind velocities in reference to the DL and DCR measurements). Interpretations of these however must account for this partial measurement of the vector field. During OCAL, the DL sampled the wind along 6 range-height indicator (RHI) scans in 6 azimuthal directions ( $0^\circ$ ,  $30^\circ$ ,  $60^\circ$ ,  $90^\circ$ ,  $120^\circ$ , and  $150^\circ$ ) and along two  $360^\circ$  plane-position indicator (PPI) scans with elevation angles of  $0^\circ$  and  $45^\circ$ . The scan pattern is illustrated in Figure 2. The RHI scans were performed between  $-5^\circ$  and  $185^\circ$  elevation angles, i.e.  $-5^\circ$  under the horizon. The scan speed was  $3^\circ/\text{s}$  and with an integration time of 1 s and an angular resolution of  $3^\circ$ . Data were stored up to a range of 12 km with a range resolution of 30 m and the first reliable data point was at a distance of 60 m but the maximum range depends on the atmospheric conditions (number of scatters needed to produce a sufficiently high signal-to-noise ratio, and atmospheric attenuation of the laser radiation). The full scan pattern was timed to be repeated every 15 minutes. The DL operated fully autonomously and continuously, even during precipitation and severe weather events, with no operator intervention required. With a remote connection, the system status and the measurement configuration could be supervised and data could be downloaded. ‘Quick-look’ images were created in real time and uploaded to a server to be used also by other project partners, and for quality control. For analyses, we stored and assessed the Doppler velocity, the backscatter coefficient, and the signal-to-noise ratio.

Measurement period: Jul 2017-Apr 2019. Data availability was  $>70\%$ . The DL sensor was maintained between 31 August 2017 and 1 February 2018 by HALO Photonics in the UK. Additionally, there were three short measurement interruptions ( $< 24$  hours) due to power cuts, after which, immediate automatic rebooting took place under remote and local supervision. More details of DL specifications and operation can be found in Table A1 in the Appendix.

### **2.2.2. Doppler cloud radar (DCR)**

The DCR instrument is a MIRA-35 Doppler cloud radar (Görsdorf et al., 2015) which operates on a Ka-band frequency of 35.1 GHz, and is developed and manufactured by Metek GmbH. Due to its longer wavelength, the radar signal is sensitive to larger objects than the DL such as larger cloud droplets, raindrops, and ice crystals. Consequently, it extends the velocity measurements to the insides of clouds where the DL signal is quickly blocked. Therefore, the DL and DCR measurements complement each other. The main technical specifications of the MIRA-35 radar are listed in Table 1.

The DCR has a movable scanner unit allowing the beam to be orientated freely in all directions. Similar to the lidar, the measured wind velocity of the DCR is in line-of-sight with respect to the radar beam. The performed scan pattern was synchronized to that of the DL as closely as possible both directionally and chronologically. Six RHI scans (azimuth of  $0^\circ$ ,  $30^\circ$ ,

60°, 90°, 120°, 150°) and two PPI scans (5°, 45°) were executed every 15 minutes. The first PPI scan was set with an elevation angle of 5° because the nearby roof, on which the DL was placed, would have blocked the radar beam set at an 0° elevation. The scan speed was 3°/s and with an integration time of 1 s and an angular resolution of 3°. Data were stored up to a range of 15 km with a range resolution of 30 m and the first reliable data point was at a distance of ~60 m. Once deployed, the DCR was set to operate autonomously and continuously with minimal operator intervention. System status and alarm messages were sent via internet connection, facilitating daily supervision of the system. As for the DL, ‘quick-look’ images were created in real time and uploaded to a server to be used also by other project partners and for quality control.

For our analyses, we recorded the Doppler velocity and radar reflectivity. Other data products of the system like peak width, linear depolarization ratio and skewness were also stored.

Measurement period: Jul 2017-Apr 2019. Data availability was >95%. There was a break for a cable repair between 3 October 2018 and 31 October 2018. Additionally, there were three short measurement interruptions (< 24 hours) due to the aforementioned power cuts, after which, immediate automatic rebooting took place under remote and local supervision). More details of DCR specifications and operation can be found in Table A1 in the Appendix.

### 2.3. Selection of measurement site

The site for the OCAL Observatory was selected first and foremost on a scientific basis, but also with some necessary logistical considerations. We developed our meteorological and geophysical criteria in a way that would best meet our objectives – namely, to observe both the pre-convective environment and the orographic processes leading to CI, including valley flows and convergence lines. Our criteria for an ‘optimal’ site were as follows:

- Moist convection should ideally occur several times within the project timeframe. Therefore, there should be occasional CI events occurring around the observatory, determined statistically through observations.
- To observe low-level convergence lines, the observatory should be in a prominent position with a clear viewpoint in many directions, to allow for measurements down to 0° and even negative elevation angles.
- The observatory location should be representative of the Al Hajar Mountain climate. It should therefore not be situated where very unusual conditions exist, such as on a very high peak, close to a particularly large valley or the ocean, or toward the edge of the mountains.

Technical and project-related prerequisites were that the observatory should have:

- A high-elevation location in the Al Hajar Mountains, within the UAE, accessible by road with (mostly) unblocked hemispherical view

- Access to a reliable power source including 3-phase AC electricity (for the DCR)
- Access to a telecommunications network for monitoring and data retrieval

With these criteria in mind, we selected seven candidates for a suitable site, initially through analysis of satellite imagery, and subsequently via terrestrial and low-level aerial surveys.

The candidate sites are shown together alongside the aforementioned detected summer CI events from Branch et al. (2020), in Figures 3a and 3b. It can be seen that several, though not many, CI events were detected in the region of the measurement sites in the summers between 2010 and 2016. Most CI events occurred to the west and south of the measurement sites (3a and 3b).

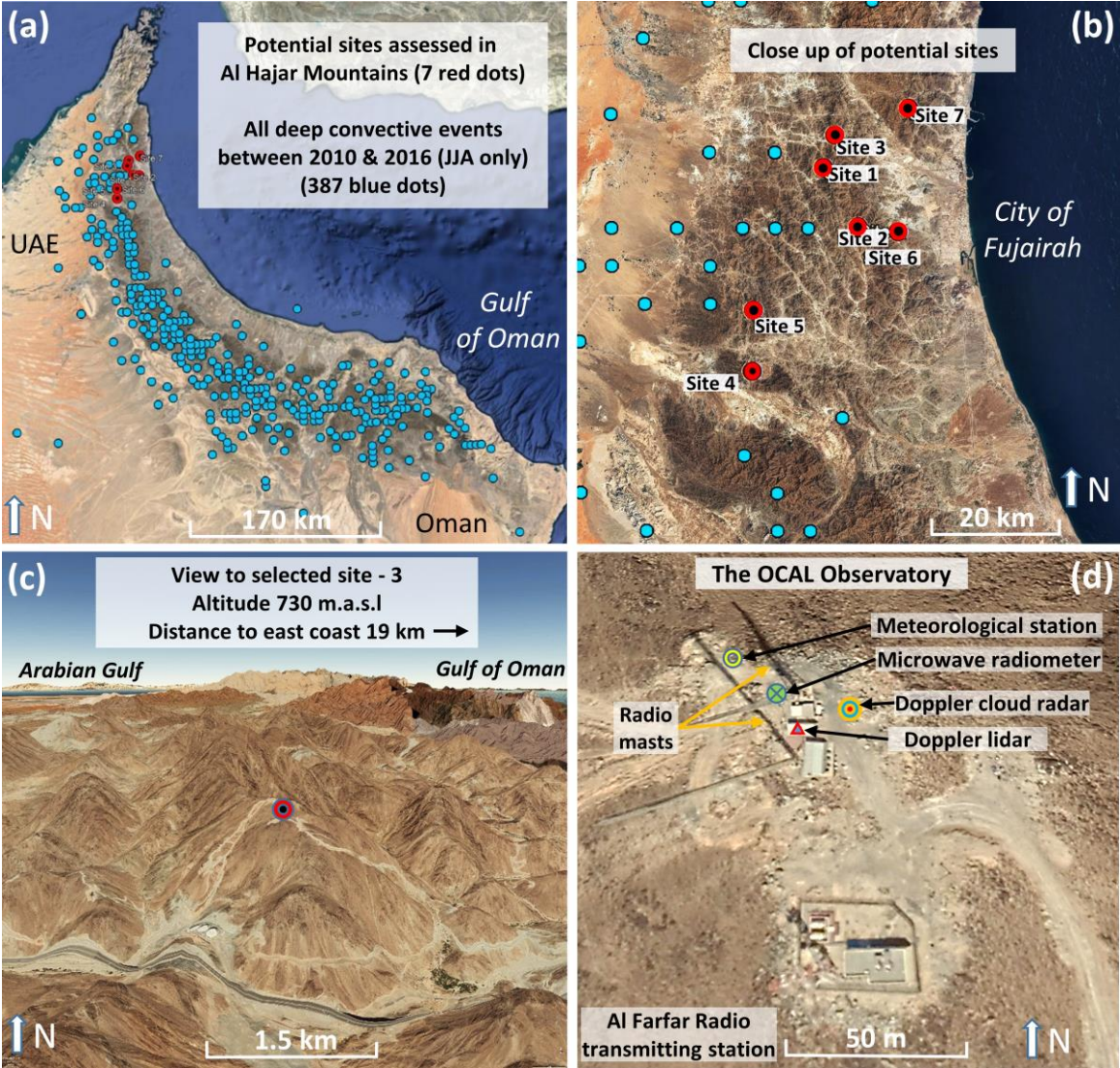


**Figure 3: Images of Al Hajar Mountains in the eastern United Arab Emirates and northern Oman (panel a). Marked in red are the candidate measurement sites initially chosen for surveys and final selection. Marked in blue are summer convective initiation events as detected from Meteosat data for 2010-2016. Marked in green are the cities of Fujairah and Al Ain in the UAE. Panel b shows a close-up view of the**

candidate sites. Panel c shows a 3D view of the chosen site looking north (site 3 from panel b). Panel d is a layout of the observatory including radio station and transmission towers, and instruments. Background imagery taken from Google Earth Pro (2020).

Several proposed sites were discounted after due consideration. Site 2 was available but had no power source. Sites 6 and 7 likewise, were deemed to be too close to the coast to be optimal and Sites 4 and 5 were located in sensitive military areas close to the border of Oman, and as such permissions were not available. Furthermore, Site 4 was considered to be sub-optimal because it sits at the north edge of a broader, deeper valley running east-west (Figure 3b). It was feared there might be a dominating influence by this valley, and it would be less representative of the mountain terrain overall. This influence from larger valleys may indicate why one of the broadest valleys, situated to the south, east of the city of Al Ain (marked in green on Figure 3a) had the highest observed density of summer CI events in the Al Hajar Mountains between 2010-2016. This valley, although interesting scientifically, is situated outside of the UAE though.

With consideration of all criteria, we finally selected Site 3 as the best candidate. This is the Jabal Umm al Farfar peak at 730 m above sea level at 25.1662°N, 56.1758°E in the emirate of Fujairah (site henceforth named Al Farfar). Al Farfar is located higher than most nearby mountains, allowing a remarkably unrestricted horizon-viewpoint in most directions for at least 2-3 km (see Figure 3c), the only exception being a slightly higher peak to the north 2 km away at 25.1844°N, 56.1703°E, which is ~850 m.a.s.l and a peak of similar height 2 km to the south-south-east. Because of its prominent location, and position in relation to the city of Fujairah, Al Farfar houses a radio transmission station for the Fujairah FM radio station. This comprises several permanently-staffed buildings and 2 large transmitter towers - the highest of which is 110 m tall (see Figure 3d). Such towers of course mean a slight obstruction, but the blockage is relatively narrow and can be accounted for when interpreting the output of the instruments. On the other hand, having such an installation there provided a big advantage in terms of in-situ infrastructure like power, communications, access, security, support in instrument maintenance, and thankfully permissions. Al Farfar sits on the northern edge of an east-west orientated valley which links the desert plains in the west with the city of Fujairah on the east coast, via a road which traverses ~34 km through the mountains. Being situated halfway along this pass (the coast is 19 km away) it was deemed to be not too close to the coast or to the desert to the west as to be unrepresentative of the mountain terrain. Additionally, although Al Farfar is connected to the coast by the valley, it is relatively narrow and not so deeply cut into the mountains. Because of this limited scale, it was judged at the time that the valley should not likely be an overly dominant effect on CI.

In summary, Al Farfar was judged to offer the best all round position from a scientific viewpoint, i.e., i) a prominent viewpoint in most directions, ii) good representativeness in terms of the mountain terrain and iii) situated far enough west to have a good chance of observing CI events (as detectable using the Meteosat MFG method of Branch et al. (2020). From a logistical viewpoint, it offered excellent infrastructure for a substantial campaign – albeit with an extremely challenging access road for delicate instruments.



### 2.3.1. Installation and positioning of instruments at observatory

The transport and installation of the instruments to Al Farfar was extremely challenging due to the poor access road, which is extremely steep, at times exceeding a 1:2 slope. Furthermore, the road was occasionally damaged and made impassable by flash floods and needed to be repaired. Consequently, the surface was very uneven and our approach toward the mountain top needed to be very slow to protect the delicate instrumentation (> one-hour drive from the mountain base to the top). Images of the transport of the DCR to Al Farfar are shown in Figure 4a and 4b.

The final positioning of the DL and DCR at the observatory are shown in Figure 4c and 4d and also in Figure 3d. The DL was installed on a single-story flat roof to provide the best possible vantage point, with the correct orientation in respect to magnetic north (Figure 3, left). The DCR was positioned within 20 m of the DL, and was also orientated in respect to magnetic north (Figure 4d). The final positions of both instruments were adjusted to avoid blocking by the large radio towers with respect to the vertical RHI scans. Some blocking during the PPI scans was naturally unavoidable, and this was taken into account during the interpretation of images.



**Figure 4: Images of the transport of the DCR and the final positions of the DL and DCR on site. Panel (a) shows the night time transport of the DCR scanner up to Al Farfar at 01:08 local time. Panel (b) shows the loading of the DCR trailer onto the AWD vehicle at NCM in Abu Dhabi, before transport to the mountains. Panels (c) and (d) show the final positions of the DL and DCR respectively, with the white arrows showing approximate compass headings. The personnel involved in the transport, shown in panel (b), are pixelated for privacy reasons.**

## **2.4. Other datasets used for analysis**

### **2.4.1. Soundings**

Standard radiosonde data were taken from the twice-daily launches at Abu Dhabi International Airport. They were available at both 00:00 and 12:00 UTC (04:00 and 16:00 local-time (LT)). The launching station is 174 km away to the west of the OCAL field observatory, and with a lower elevation, but this was the closest available data. The radiosonde data was obtained from the Department of Atmospheric Science at the University of Wyoming in the United States. As well as deriving a Skew-T diagram from the radiosonde data, we extracted convective available potential energy (CAPE), convective inhibition (CIN), and precipitable water (PWAT) to characterize the stability of the atmosphere along the radiosonde track.

### **2.4.2. Geostationary Satellite Imagery**

In order to provide wide gridded coverage of the distribution of clouds, High Rate Level 1.5 Image Data was taken from the SEVIRI sensor aboard the Meteosat-8 (MSG) geostationary satellite, situated equatorially at a longitude of 41.5°E over the Indian Ocean. Two channels were used to assess the presence of clouds and corresponding brightness temperatures: the High-Resolution Visible [HRV] channel at a wavelength of 0.6  $\mu\text{m}$  ( $\Delta x \sim 1$  km) the infrared (IR) channel at a wavelength of 10.8  $\mu\text{m}$  ( $\Delta x \sim 3$  km).

### **2.4.3. ECMWF operational analysis model data**

To show the synoptic weather situation, we assessed geopotential height at 500 hPa, U and V components at 850 hPa and column integrated water vapor. These fields were retrieved from the European Centre for Medium-Range Weather Forecasts (ECMWF) Integrated Forecasting System (IFS), in the form of 6-hourly operational analysis data on the 41r1 cycle, on standard pressure levels. The model horizontal grid increment is 0.125° ( $\sim 12$  km) with 137 vertical levels up to 0.01 hPa.

### **2.4.4. ECMWF ERA5 Reanalysis data**

To show the static stability of the atmosphere during our two cases, convective available potential energy (CAPE) was used. We retrieved this field from the European Centre for Medium Range Weather Forecasting (ECMWF) ERA5 reanalysis dataset. ERA5 is derived from the ECMWF Integrated Forecasting System (IFS), and employs a horizontal grid spacing of 0.28125° or  $\sim 30$  km. The model data is then retrospectively corrected with observations (Hersbach et al., 2020).

### **2.4.5. UAE precipitation radar network**

To provide a wider context for our measurements and show precipitation in conjunction with the cloud radar measurements, we retrieved reflectivity data from the National Center for



Meteorology (NCM) C-band precipitation radar network (5596-5622 MHz). Vertical resolution is 0.75 km with a horizontal resolution of 500 m. The location and range of the radars are shown in Figure 5. Detailed technical and historical information on the UAE radar network can be found in a report by NCAR (2005).

Figure 7b indicates a large land-based heat low over the western Arabian Peninsula which is typical for this hot desert. This low-pressure draws southerly-westerly winds over the UAE. Integrated water vapor is 27-30 mm m<sup>-2</sup> over the north-eastern UAE coast indicating moderately high moisture in the atmosphere. Figure 7c shows very high static instability indicated over the Gulf of Oman and the north-eastern tip of the UAE, with CAPE values of up to 7000 J kg<sup>-1</sup>. These quantities indicate that even though conditions further to the west were stable (e.g. in the city of Abu Dhabi), the atmosphere close to the OCAL observatory was strongly primed for moist convection.

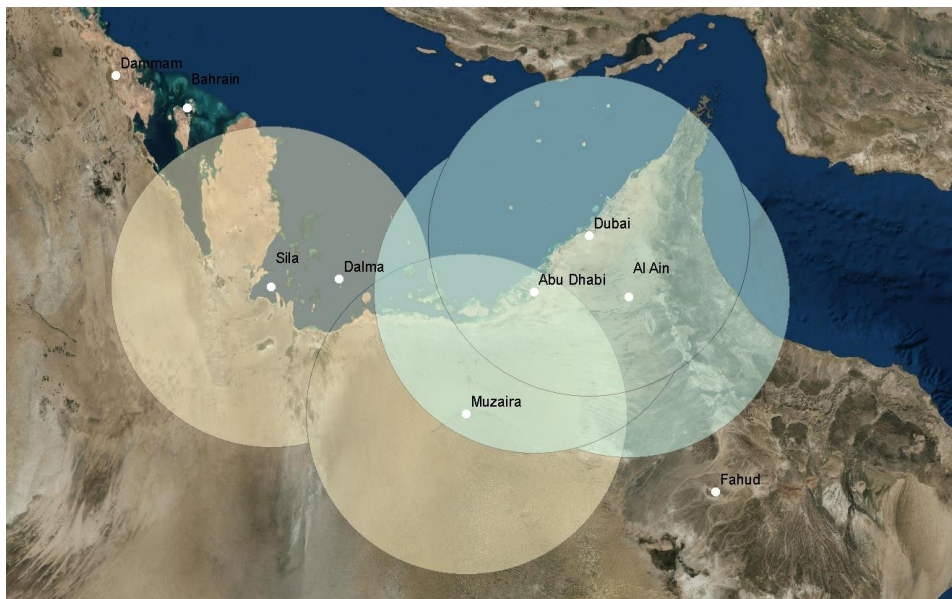


**Figure 5: Location of UAE C-Band precipitation radar network with 6 radar sites. Three of those sites overlap with the Al Farfar measurements observatory – Abu Dhabi, Al Ain, and Dubai.**

### 3. Results

#### 3.1. Case studies

Here we present two interesting cases – the 6 September 2018 which was a relatively strong convective case and the 5 September 2018 which is a weaker convective event. These were selected, based on analysis of the lidar and cloud radar quick-look images, alongside satellite and ground precipitation radar imagery. A central focus of this analysis is to compare what insights can be gleaned from readily available data during these convective cases, with those gained from high resolution observations at the observatory – particular in respect to convective process and the pre-convective environment. Hence for each case, we present first

analyses of satellite imagery and precipitation radar, followed by observations from the DL and DCR.

### 3.1.1. The 6 September 2018 – a stronger convective case

**Satellite and precipitation radar** - on the 6 September, scattered convective cells appear over the northern Al Hajar Mountains, with a large precipitating convective cloud developing over the OCAL observatory at ~9:00 to 9:30 UTC (13:00 to 13:30 LT). This can be seen in Figure 6. The Meteosat HRV visible channel shows a small cloud appearing just to the south-west of the OCAL observatory at around 8:30 UTC (6a). In the previous time step (8:15) there are no clouds visible nearby. At both of these times, the Meteosat brightness temperature (BT) (derived from 10.8  $\mu\text{m}$  channel radiances) is 309.5 K directly over the observatory. At 9:00 UTC, the cell strengthens and appears directly over the observatory (6b), and the BT drops to 273.0 K. At 09:15 it drops further to 266.2 K. In the precipitation radar imagery, the first signal only appears at 09:30 (6c) with a maximum reflectivity of 45 dBZ near the observatory.

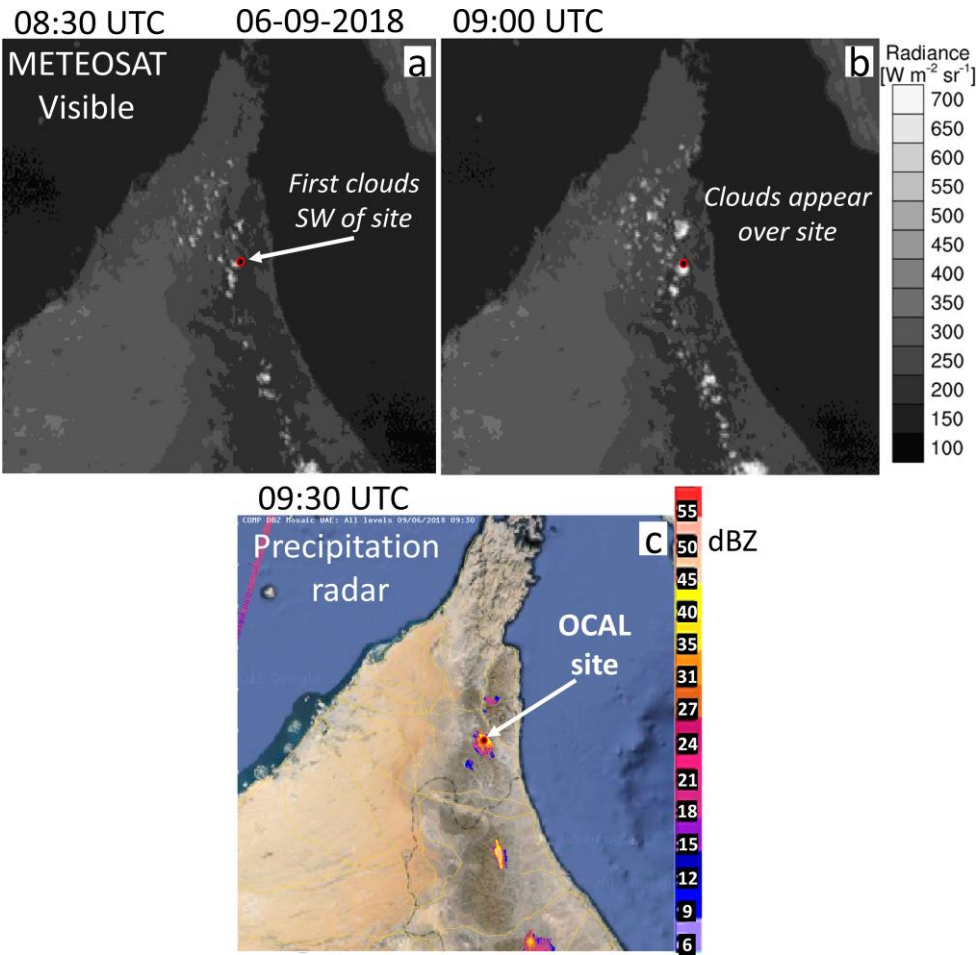


**Figure 6: Satellite imagery (top panels (a) and (b)), and ground-based precipitation C-band radar (bottom panel (c)) on 6 September 2018. The satellite imagery is based on Meteosat-8 SEVIRI sensor data and shows the High Resolution Visible (HRV) channel (0.6  $\mu\text{m}$ ) in greyscale. The C-band precipitation radar images show the vertical-maximum reflectivity [dBZ] as derived from 20 measured levels.**

**Weather situation, from ECMWF operational analysis and ECMWF ERA 5 reanalysis model data** – The 00:00 UTC radiosonde profile from Abu Dhabi Intl. Airport (Figure 7a) indicates warm surface temperatures at  $>32^{\circ}\text{C}$  with low surface humidity at  $\sim 7\text{--}10\text{ g kg}^{-1}$ , which dries off rapidly with height. Surface winds are southerly. There is a fairly stable environment with a high level of free convection (LFC) at roughly 600 hPa, and CAPE and CIN values are close to zero and with a moderate column PWAT of 23.2 mm. We selected the preceding radiosonde to the first cloud appearance (on 6 September  $\sim 9\text{:}00$  to  $9\text{:}30$  UTC) to assess the pre-convective environment. However, this is nine hours after the launch. Given the time lag and the 173 km distance to the launch site, the radiosonde can only provide a coarsely representative picture of the pre-convective environment in the region. Panel 7a shows the synoptic weather situation based on ECMWF analysis data, and panel 7b shows atmospheric static stability (CAPE) over the east coast of the UAE and the OCAL observatory at 08:00 UTC, based on ECMWF ERA5 data. The time of 08:00 UTC is approximately one hour before the first appearance of clouds near the observatory and so provides an overview of the pre-convective environment.

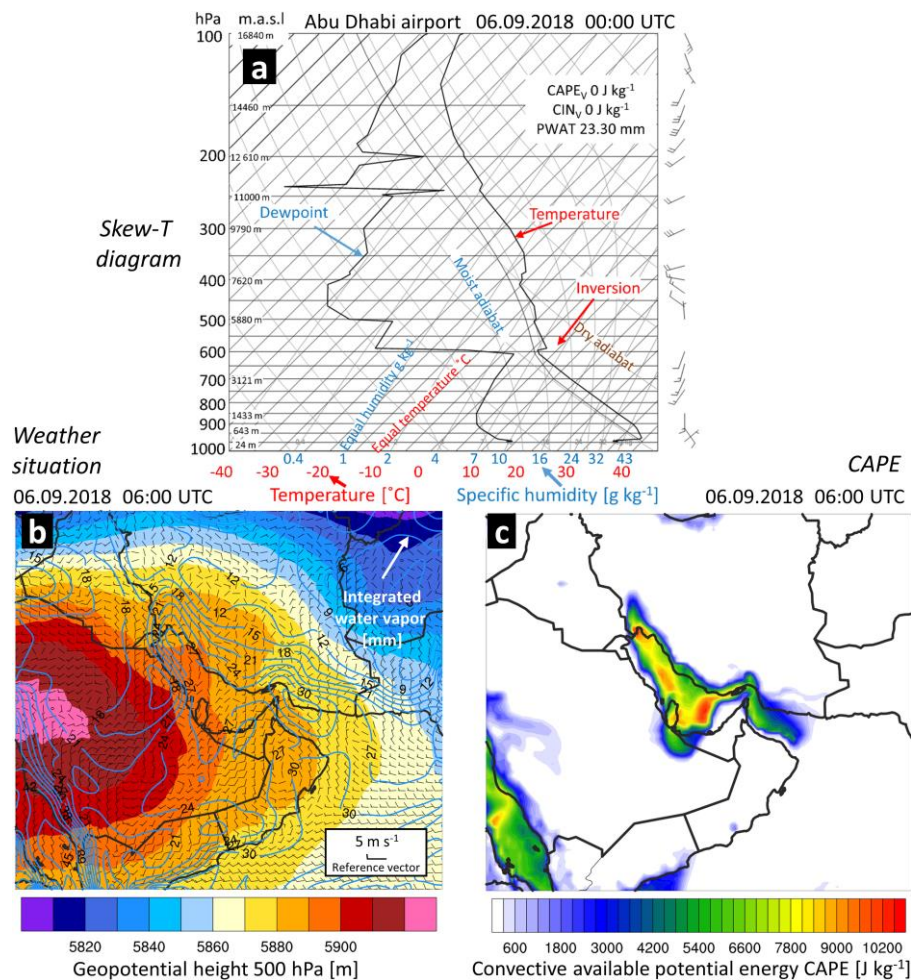


**Figure 7: Weather situation for 6 September 2018, as illustrated by a Skew-T diagram (panel a), and synoptic meteorology (panels b and c). The Skew-T diagram shows vertical profiles of virtual temperature (right bold curve) and dew point (left curve) at 12:00 UTC – measured by radiosonde at Abu Dhabi**

International airport. CAPE is the area bounded on each side by the non-bold right curve and the parcel path. Isopleths of temperature, mixing ratio, moist/dry adiabats, and total CAPE/CIN and precipitable water (PWAT) are indicated. The synoptic situation (b), was derived from ECMWF operational analysis data, and shows geopotential height at 500 hPa (filled contours) [m.a.s.l], wind barbs at 850 hPa [ $\text{m s}^{-1}$ ] and integrated water vapor [mm] – at 06:00 UTC. Panel (c) shows virtual CAPE based on ERA5 data [ $\text{J kg}^{-1}$ ] – at 06:00 UTC.

Figure 7b indicates a large land-based heat low over the western Arabian Peninsula which is typical for this hot desert. This low-pressure draws southerly-westerly winds over the UAE. Integrated water vapor is 27-30  $\text{mm m}^{-2}$  over the north-eastern UAE coast indicating moderately high moisture in the atmosphere. Figure 7c shows very high static instability indicated over the Gulf of Oman and the north-eastern tip of the UAE, with CAPE values of up to 7000  $\text{J kg}^{-1}$ . These quantities indicate that even though conditions further to the west were stable (e.g. in the city of Abu Dhabi), the atmosphere close to the OCAL observatory was strongly primed for moist convection.

**Observations at the OCAL observatory** – Figure 8 shows selected PPI and RHI scans from the DL just around the time of the first cloud development close to the observatory on the 6 September. The range shown is 5 km which exceeds the DL range on this day – determined both by the amount of aerosol particles required for backscattering, the atmospheric extinction, and the laser’s performance. Figures 8a to 8c show PPIs at a  $0^\circ$  elevation. The red colors in all scans indicate a line-of-sight velocity in a direction away from the lidar, and a blue color is towards the DL. A white color indicates either very low or zero wind speeds, or more likely a wind direction which is normal to the laser beam. If these transitions occur at the position of the lidar, e.g. directly at the PPI center, this would only indicate the change in laser beam direction with respect to mean wind flow. If it occurs away from the DL then this can indicate wind shear or convergent/divergent flows. From 8a, we can see that the mean surface wind direction is generally from an easterly direction. Panels 8a to 8c show a flow distortion around 1.5-2 km to the south-south-west of the lidar (indicated by black circles), which is almost certainly due to the presence of a mountain peak slightly higher than the observatory (8d). It appears that the easterly valley flow directly south of the observatory is distorted here creating a convergence line as the winds flow over and around this obstruction. Such orographic flows can provide a lifting mechanism which can initiate convection in the right conditions (e.g. Behrendt et al., 2011; Smith et al., 2014). Figure e-g show vertical RHI scans on roughly the same azimuthal plane toward this hard target ( $30^\circ$ ) and we can observe the steady development of an updraft over the lidar between 8:46 and 09:17 UTC (also circled) which corresponds approximately with the distance to this flow distortion, in panels 8a to 8c. We may surmise then this updraft is directly attributable to the flow distortion.



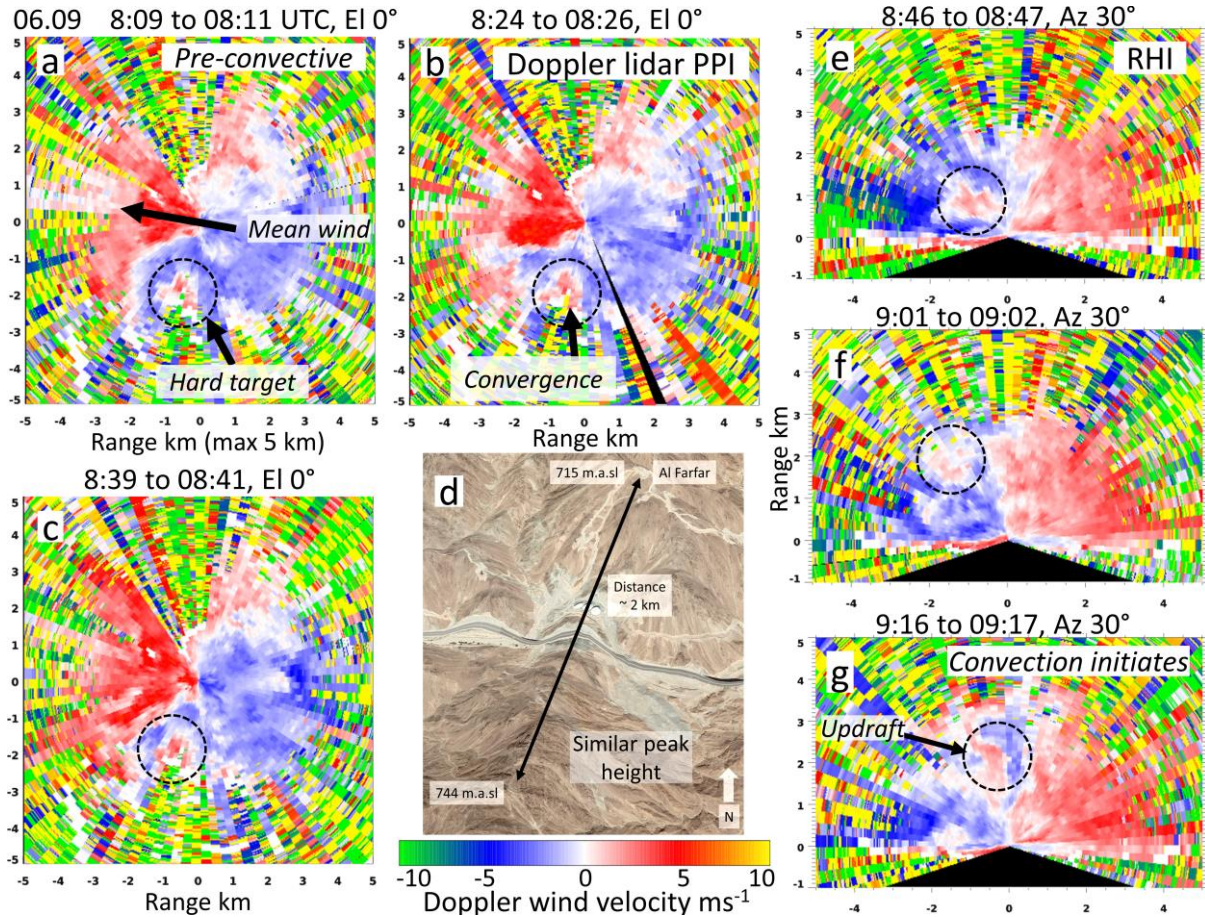


**Figure 8: Doppler lidar PPI (El 0°) and RHI (AZ 30°) wind velocity scans on the 6 September 2018. Also shown is the relative position of a peak of similar elevation (hard target) ~2 km south-south-west from the OCAL observatory.**

Figures 9 and 10 show images from the DCR which require larger droplet sizes to provide a Doppler signal (note the difference in the plotted DL and DCR ranges). with a signal indicating the presence of clouds and/or falling hydrometeors. Rapid velocities within or below clouds can therefore reflect the fall speeds of hydrometeors – again assuming line of sight velocities. Figure 9 shows corresponding PPI images with elevation angles of 0° and 45° (panels a to c, and d to f, respectively). Panel 9a shows no signal at 8:53 UTC meaning there are no clouds or hydrometeors reaching the observatory level. Panel 9b shows the first signal to the west of the DCR. This also corresponds to the visible satellite image where a cloud forms to the west and south (Figure 6a). In 9e we can see the increasing development of clouds toward the west and south with line of sight fall velocities of 5-10 m s<sup>-1</sup>. These hydrometeors start to reach the ground at 9:08 UTC (9b). At 9:26 UTC we see the presence of a significant single cell over the DCR with up and downdrafts of at least 10 m s<sup>-1</sup> with a widespread area of precipitation at the ground (9c). The initiation and depth of this cell can be seen in the 30° RHIs in Figure 10. Figure 10a shows the time just before CI is apparent in this plane (09:00 UTC) and the subsequent appearance of the cell which reaches up to 8 km in height (10b), along with strong updrafts above 4 km height and greater downdrafts and fall

speeds below 4 km. Interestingly, the position and direction of this cell (1.5-2km,  $\sim 210^\circ$  from north) corresponds to the direction and distance of the hard target (as seen also in Figure 9e).

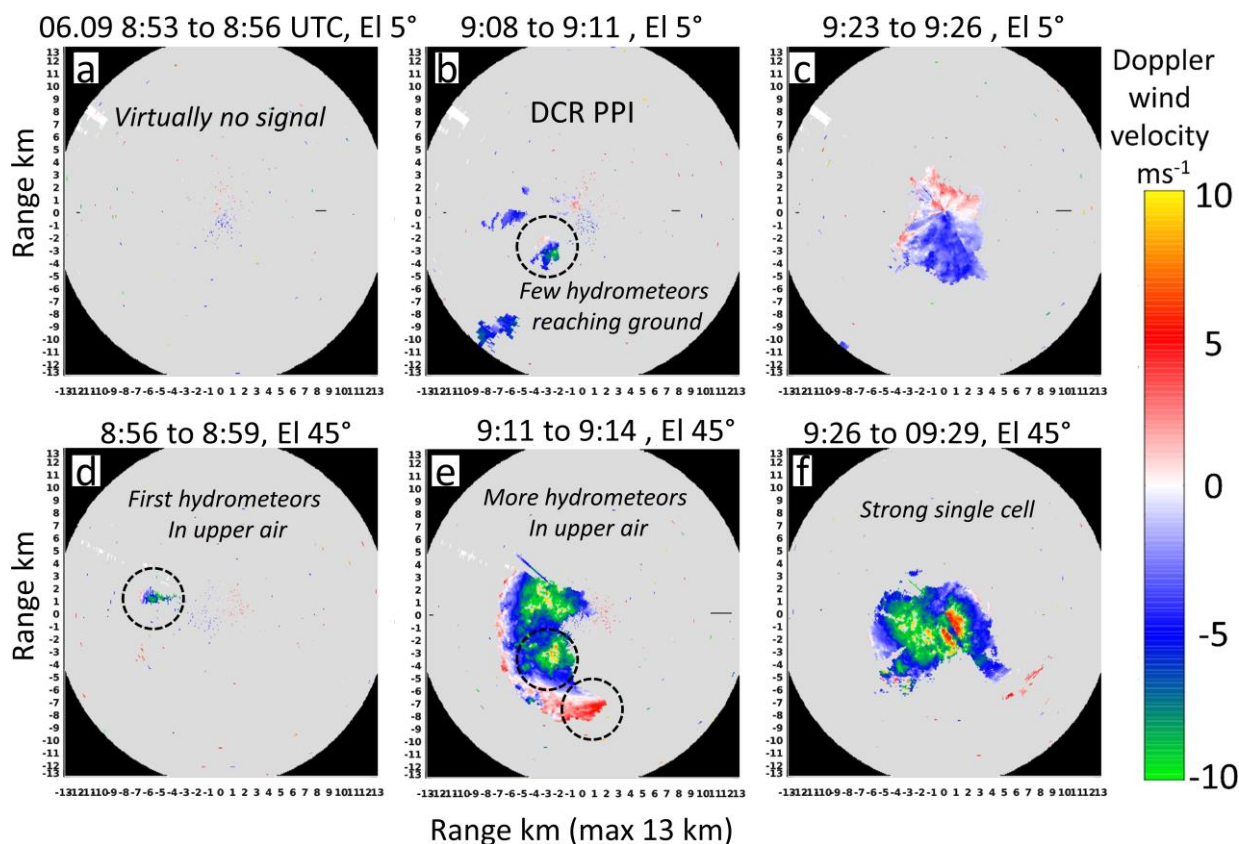


**Figure 9: PPI velocity scans ( $5^\circ$  and  $45^\circ$ ) from the DCR on the 6 September 2018.**

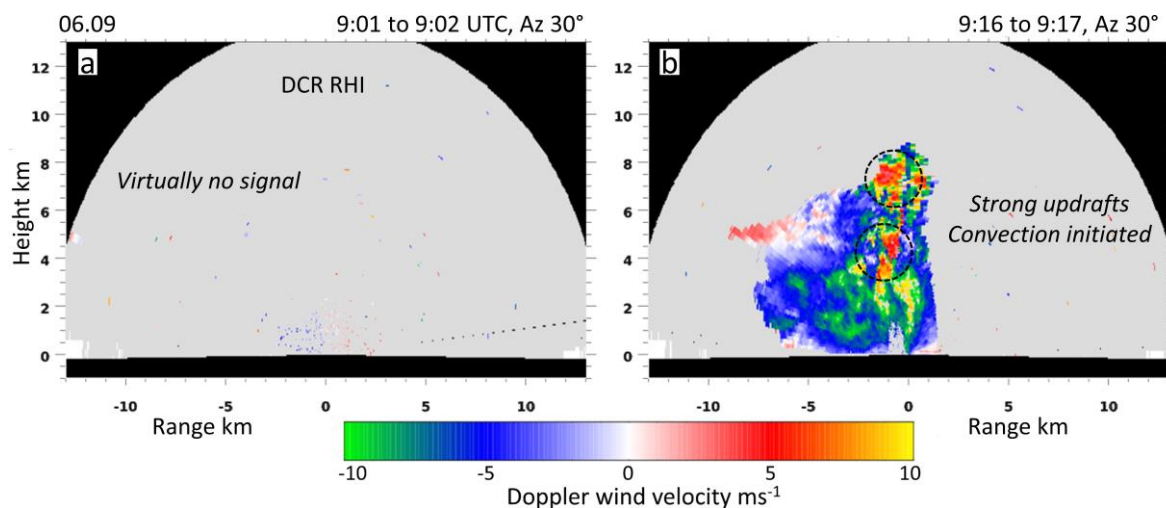


**Figure 10:  $30^\circ$  RHI velocity scans from the DCR on the 6 September 2018.**

In this case study, we can observe from the DL scans in Figure 8 that there were already strong signs in the pre-convective clear air environment that CI may occur. This was even before the first signs of hydrometeors in the DCR at around 9:00 UTC and certainly long before precipitation becomes visible in the C-band radar at 9:30 UTC (6c). Figure 8e clearly



shows the onset of strong updrafts 10-15 minutes before clouds develop (see also Figure 9d to 9e). We may surmise that the visible low-level flow distortion was the decisive trigger of the development of the cell and its position, with upper air phenomena in the wider region providing the overall conditions required for CI.

### 3.1.2. The 5 September 2018 – a weaker convective case

**From satellite and precipitation radar** – on the 5 September, two faint convective cells appear in the HRV visible channel to the south of the OCAL observatory at ~10:15 UTC (14:15 LT) (Figure 11). A stronger cell develops over and to the south of the OCAL site at 11:15 UTC (observatory BT is 287.4 K). These cells dissipate, or move away and then another larger cell is apparent over the observatory at 12:15 UTC (11d). At this point the observatory BT is 291.5 K, which indicates a lower cloud height than at 11:15 UTC. However, the 10.3  $\mu\text{m}$  channel has a 3 km spatial resolution in contrast with the 1 km HRV channel, and hence some error might be expected in terms of strong but isolated cells. In the C-band precipitation radar imagery, there is only a single faint signal at 12:36 UTC (11d) in a small patch to the south of the observatory, and this only shows a maximum reflectivity of ~15 dBZ.

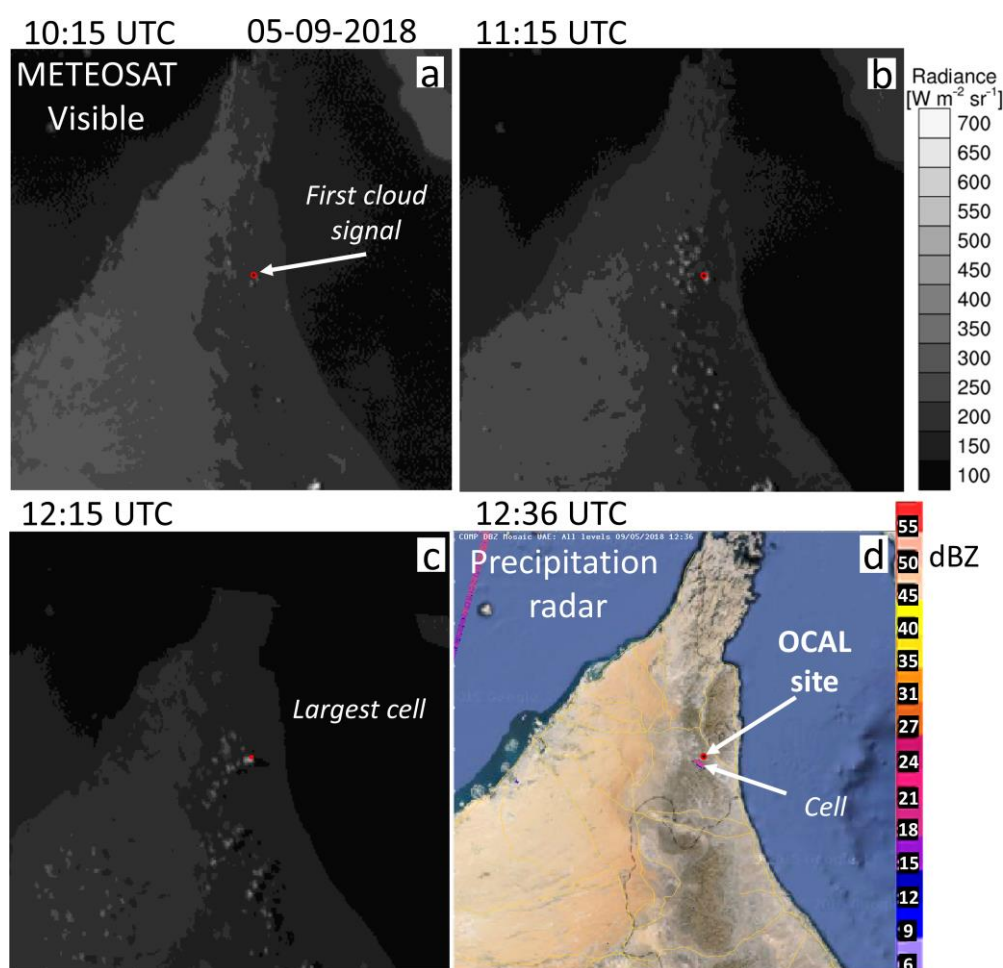
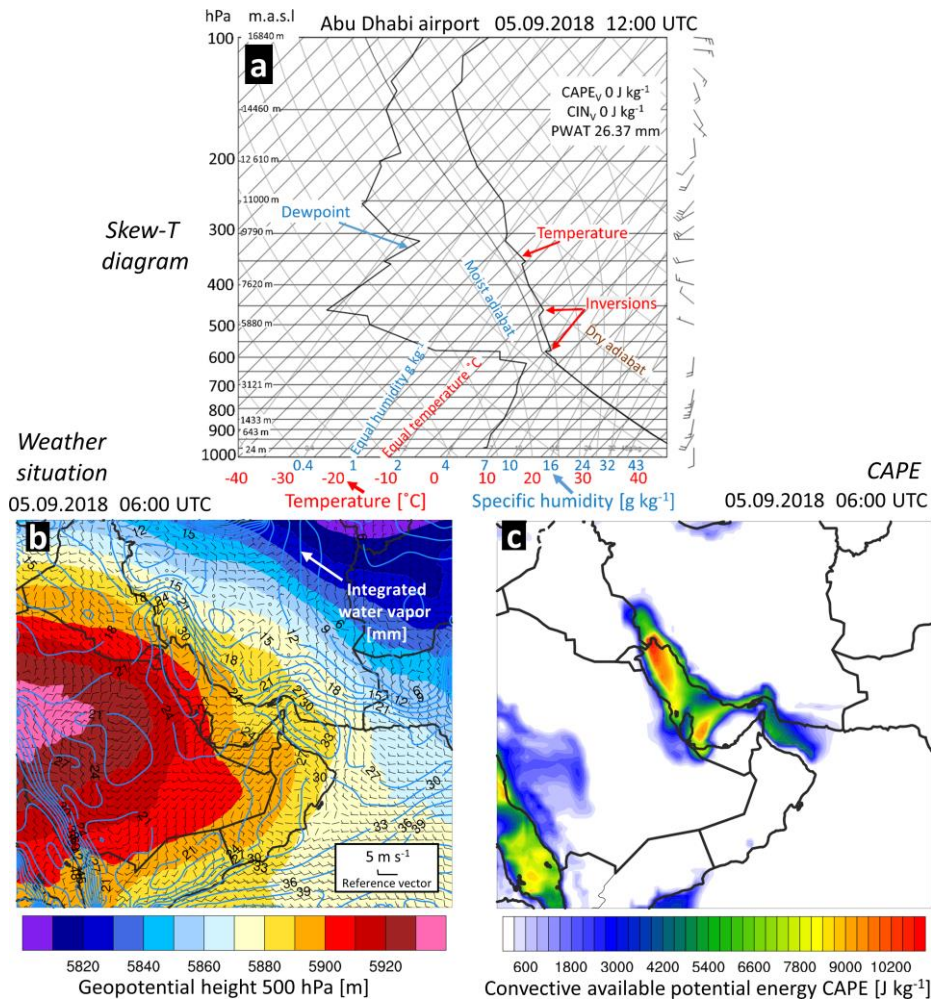


Figure 11: As for Figure 6 but for the 5 September 2018.

**Weather situation, from ECMWF operational analysis and ECMWF ERA 5 reanalysis model data** – The radiosonde Skew-T in Figure 12a shows very hot surface conditions in at Abu Dhabi Intl. Airport at 12:00 UTC, when the largest cells were observed around the observatory. The observed conditions are similar to the 6 September. The surface humidity is quite low at  $7 \text{ g kg}^{-1}$  and a statically stable atmosphere is indicated with a high LFC at 600 hPa, almost zero CAPE, and a moderate PWAT of 26.3 mm. The synoptic situation, as seen in the ECWMWF analysis data (12b), shows quite similar conditions to the 6 September – with an area of low pressure dominating the western Arabian Peninsula and south-westerly winds crossing over the eastern UAE and the Gulf of Oman. However, the integrated water vapour over the Al Hajar Mountains near the OCAL site is higher at around  $30\text{-}33 \text{ mm m}^{-2}$ . Figure 12c indicates an area of high CAPE to the east of the Al Hajar Mountains but with more moderate values - up to  $3500 \text{ J kg}^{-1}$  at the eastern UAE coast. Higher values of up to  $5000 \text{ J kg}^{-1}$  occur further out to sea. Hence, the atmosphere over the UAE Al Hajar Mountains is also primed for convection, but perhaps fractionally less so than on the 6 September. This appears to be well-reflected in the higher number and size of clouds on the 6 September (Figure 6), as compared to the 5 September (Figure 11).



**Figure 12: Daily weather situation for the 5 September 2018. All plot variables are the same as for Figure 5 except for the Skew-T plot which is at 12:00 UTC.**

**Observations at the OCAL observatory** – During this case, we observed two different occurrences of CI – one around 10:30-11:00 and one at 12:00 to 12:30. These are presented respectively in Figures 12 and 13. Figure 13 shows a series of DL and DCR PPIs and RHIs at differing elevation and azimuth angles. The mean wind direction is easterly with speeds of around 5-7 m s<sup>-1</sup> (13a). Similar to the 6 September, we can see a visible flow distortion attributable to the hard target at both low (13a) and high level (13b). The visible flow distortion at ~ 2 km in a 45° PPI indicates an impact at the same height of 2 km (because  $\tan 45^\circ = 1$ ). This indicates the potentially strong impact of moderate orography high into the atmosphere. The DCR images (13e to 13f) show the first appearance of hydrometeors (in these geometric planes) occurs sometime after 11:00 UTC, which indicates that these flow distortions were ongoing long before clouds developed. In 13b we can also see a small convergent zone almost at the PPI centre to the west of the DL. In the DL RHIs (13c to 13d) we can see some structures between 0.75 and 2 km in height to the south-west of the DL, correspondingly with that seen in the circle in 12b. These appear to be turbulent structures and wind shear. These may be attributable to the hard target impact, but this is not certain. In 13f we have marked a 60° azimuthal transect on the 45° PPI which passes through the cloud to the south-west. The cell structure is visible with areas of strong up and downdrafts are clearly seen. Figures 13e and 13g respectively, show the corresponding DCR and DL 60° RHI just before. The DCR shows the cloud base at around 3-4 km height, the size of the cloud (2-3 km wide), and the up/downdraft velocities (reaching 10 m s<sup>-1</sup>). The DL image (13g) also shows the cloud base at around 3 km height (circled). Again, we conclude that areas of flow distortion, wind shear and finally updrafts (13d) are clearly captured by the DL within the clear air environment (13a to 13d), quite some time before clouds develop at ~11:18 UTC.



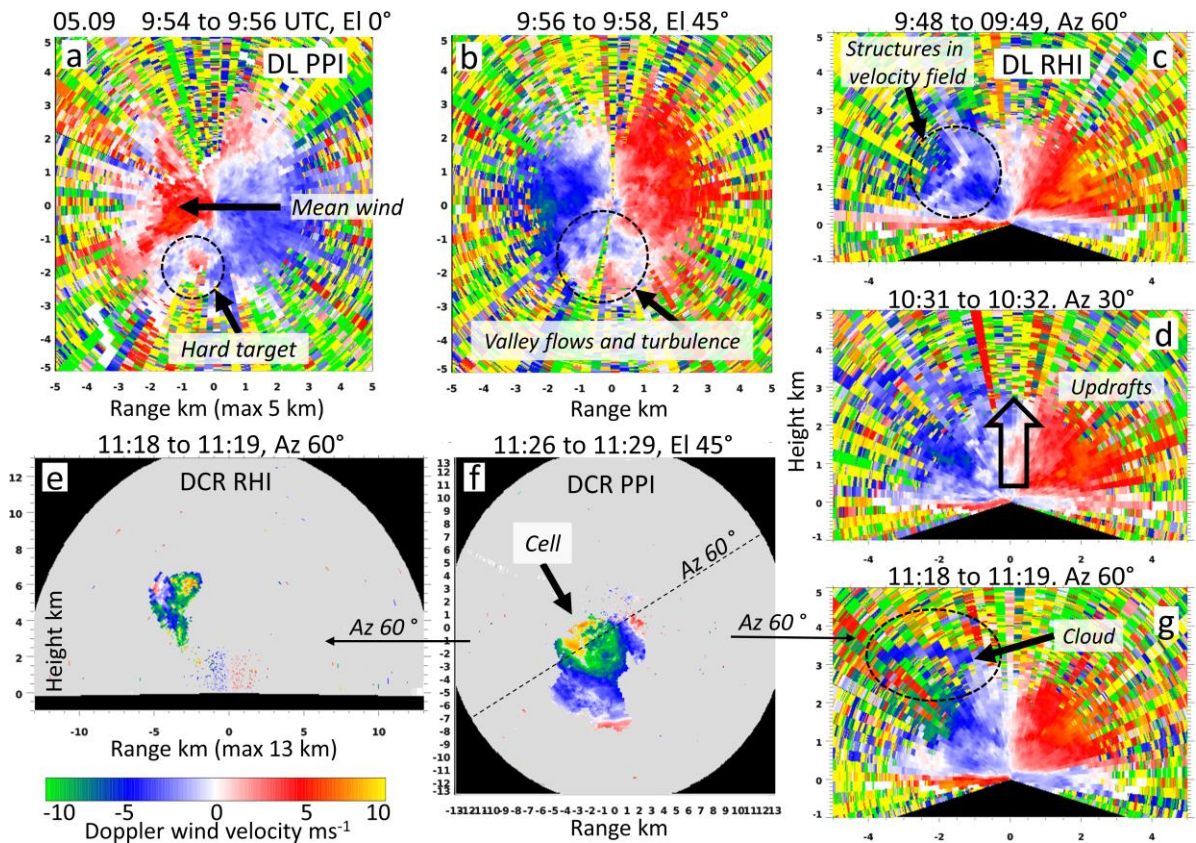


**Figure 13: Scans from the first visible cell on the 5 September (between 10:15 and 11:30 UTC). Selected RHI and PPI scans from both the DL and DCR are presented from varying angles.**

Then there is a short break where no nearby clouds are visible (Figure 14a) between 12:00 and 12:20 UTC. However, we can clearly see the continuance of some updrafts in the 30° and 60° DL RHIs directly above the observatory (14e and 14f). At 12:26 UTC, hydrometeors appear (14b) but at some distance away >3 km. At around 12:31 UTC the cell develops and moves closer to the observatory (1-2 km) (14d). At this point, updrafts reach velocities of 10 m s<sup>-1</sup> below 4 km, fall speeds reach 5 m s<sup>-1</sup> at ~4 km height, and precipitation is visible at the ground. This cloud is also clearly visible in the DL RHI at ~4 km height (14g).

Again in the DL scans, we can see dynamics in the clear air environment that precede cell development visible with the DCR. Once the cloud has developed, we can then see much more detail and structure with the DCR. In particular, the precipitation signal is seen some time before the C-band radar (11d) which only indicates light reflectivity of 15-20 dBZ, at 12:36.

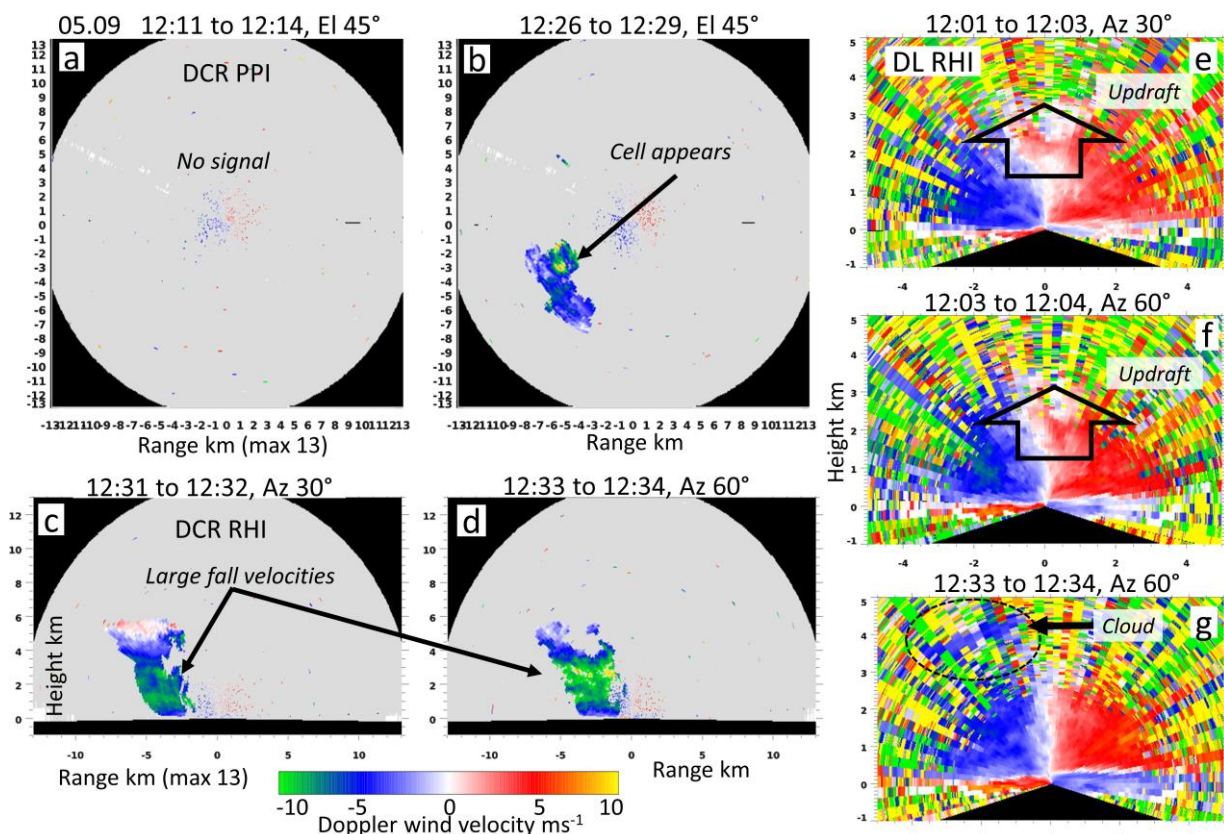


**Figure 14: Scans from the second visible cell on the 5 September (between 12:00 and 13:00 UTC). PPI (EI 45°) and RHI (AZ 60°) DCR scans and RHI (AZ 30° and 60°) DL scans from the 5 September.**

## 4. Summary

The objective of the high elevation OCAL observatory was to provide a means to investigate CI and orographic convective clouds in the Al Hajar Mountains, and the preceding clear-air environment, all well as identifying pre-convective signatures for CI. By doing so, we aim not only to improve our process understanding, particularly in respect to orographic CI, but also to provide a means of nowcasting seedable clouds – a key objective of the OCAL Project. To achieve these goals, we have employed a synergy of complementary instruments (DL and DCR), in a highly challenging arid environment, to assess dynamics in clear air and in clouds. We have compared the output with readily available satellite, radar, and model data to assess the added value of employing shorter range but higher resolution instruments to gain deeper insights into regional orographic convective cells.

We have observed that the 1 km resolution HRV channel (0.6  $\mu\text{m}$ ) of Meteosat provides a good overview of cloud development over large areas and allows us to identify convective cells with a horizontal extent  $>1$  km. However, it provides little to no information about processes occurring before or during CI. Brightness temperatures derived from the thermal infrared (10.8  $\mu\text{m}$ ) channel can be useful for tracking cell development and the identification of CI locations (e.g. Branch et al., 2020) but due to the coarser 3 km resolution of the SEVIRI sensor at 10.8  $\mu\text{m}$ , this only accounts for larger convective cells. The resolution is likely to be

improved in the proposed Meteosat Third generation. Similarly, the long-range UAE C-band radar network provides useful observations of precipitation over the whole UAE. However, we have seen that the C-band radar, suffers from blocking by the Al Hajar Mountains (Branch et al., 2020; Wehbe et al., 2020), and also tends to be rather late in identifying the onset of precipitation, when compared with the DCR for instance. This latter issue may indicate a lack of sensitivity, perhaps requiring a revision in the Z-R relationship.

The DL and DCR, using synchronized scan patterns, provide complementary insights into when and how convective cells develop, their evolution, and structure thereafter. The DL captures the pre-convective clear air dynamics at low and high levels, including the updrafts necessary for CI, and the subsequent cloud base after CI. Once cloud droplets have reached a certain size, one is then able to observe the cloud and precipitation dynamics with the DCR, alongside the DL scans.

One of the main outcomes of the study has been the identification of clear-air signatures in the DL, which occur before CI. Low-level flow distortion and convergence caused by orographic geometry can penetrate far into the atmosphere. We can deduce from the close proximity of the cell and the flow distortion, that in unstable conditions these flows are influencing CI. However, further examination is warranted to provide confirmation into the relative contribution of this valley flow to CI, e.g. under differing atmospheric conditions. We can also investigate the influence of other known regional phenomena such as horizontal convective rolls or sea breezes (e.g. see Branch et al., 2020; Francis et al., 2020; Schwitalla et al., 2020). In any case, the DL clearly captures the appearance of the updrafts some time before CI occurs, which implies that forecasting of seedable clouds with a reasonable lead time could be feasible in the Al Hajar Mountains, e.g. with a network of relatively inexpensive Doppler lidars. Such a lead time is critical for cloud seeding operations, where a latency exists between a forecast and the deployment of seeding aircraft. To increase forecast certainty, clear air DL measurements, and standard meteorological charts, could be supplemented with convective indices like CAPE or lifted index, and also more sophisticated regional indices (e.g. Branch and Wulfmeyer, 2019; Findell and Eltahir, 2003). Lidar/radar data can also be assimilated to improve the forecast system (e.g. Kawabata et al., 2018; Schwitalla and Wulfmeyer, 2014; Thundathil et al., 2020). Observations could be supplemented still further with by ground-based remote sensing (Wulfmeyer et al., 2015), especially continuous very high-resolution thermodynamic profiling with lidar (e.g. Behrendt et al., 2020; Lange et al., 2019; Späth et al., 2016). These would provide much more accurate profiles of lower and upper atmosphere at much higher spatiotemporal resolution than radiosondes or models can offer (e.g. Behrendt et al., 2011; Corsmeier et al., 2011).

In summary, this study has demonstrated the value of employing this synergy of instruments with synchronized scan patterns in a high elevation observatory for assessment of clear air and cloud dynamics. The OCAL observatory provides an excellent platform for studying the whole process chain of orographic CI within the Al Hajar Mountains, and shows potential as a timely forecasting system of seedable clouds.



## References

- Almazroui, M. (2012). Temperature Variability over Saudi Arabia and its Association with Global Climate Indices. *JKAU: Met., Env. & Arid Land Agric. Sci.*, 23(1), 85–108. <https://doi.org/10.4197/Met>
- Aoshima, F., Behrendt, A., Bauer, H. S., & Wulfmeyer, V. (2008). Statistics of convection initiation by use of Meteosat rapid scan data during the Convective and Orographically-induced Precipitation Study (COPS). *Meteorologische Zeitschrift*, 17(6), 921–930. <https://doi.org/10.1127/0941-2948/2008/0337>
- Bauer, H.-S., Schwitalla, T., Wulfmeyer, V., Bakhshaii, A., Ehret, U., Neuper, M., & Caumont, O. (2015). Quantitative precipitation estimation based on high-resolution numerical weather prediction and data assimilation with WRF – a performance test. *Tellus A: Dynamic Meteorology and Oceanography*, 67(1), 25047. <https://doi.org/10.3402/tellusa.v67.25047>
- Bauer, H. S., Muppa, S. K., Wulfmeyer, V., Behrendt, A., Warrach-Sagi, K., & Späth, F. (2020). Multi-nested WRF simulations for studying planetary boundary layer processes on the turbulence-permitting scale in a realistic mesoscale environment. *Tellus, Series A: Dynamic Meteorology and Oceanography*, 72(1), 1–28. <https://doi.org/10.1080/16000870.2020.1761740>
- Becker, K., Wulfmeyer, V., Berger, T., Gebel, J., & Münch, W. (2013). Carbon farming in hot, dry coastal areas: An option for climate change mitigation. *Earth System Dynamics*, 4(2), 237–251. <https://doi.org/10.5194/esd-4-237-2013>
- Behrendt, A., Pal, S., Aoshima, F., Bender, M., Blyth, A., Corsmeier, U., et al. (2011). Observation of convection initiation processes with a suite of state-of-the-art research instruments during COPS IOP 8b. *Quarterly Journal of the Royal Meteorological Society*, 137(SUPPL. 1), 81–100. <https://doi.org/10.1002/qj.758>
- Behrendt, A., Wulfmeyer, V., Senff, C., Muppa, S. K., Späth, F., Lange, D., et al. (2020). Observation of sensible and latent heat flux profiles with lidar. *Atmospheric Measurement Techniques*, 13(6), 3221–3233. <https://doi.org/10.5194/amt-13-3221-2020>
- Böer, B. (1997, January 1). An introduction to the climate of the United Arab Emirates. *Journal of Arid Environments*. Academic Press. <https://doi.org/10.1006/jare.1996.0162>
- Branch, O., Warrach-Sagi, K., Wulfmeyer, V., & Cohen, S. (2014). Simulation of semi-arid biomass plantations and irrigation using the WRF-NOAH model - a comparison with observations from Israel. *Hydrology and Earth System Sciences*, 18(5), 1761–1783. <https://doi.org/10.5194/hess-18-1761-2014>
- Branch, O. & Wulfmeyer, V. (2019). Deliberate enhancement of rainfall using desert plantations. *Proceedings of the National Academy of Sciences of the United States of America*, 116(38), 18841–18847. <https://doi.org/10.1073/pnas.1904754116>
- Branch, O., Behrendt, A., Gong, Z., Schwitalla, T., & Wulfmeyer, V. (2020). Convection Initiation over the Eastern Arabian Peninsula. *Meteorologische Zeitschrift*, 67–77. <https://doi.org/10.1127/METZ/2019/0997>
- Breed, D., Brintjes, R., Salazar, V., & Jensen, T. (2007). *NCAR Feasibility Studies For Weather Modification Programs Over The Past 10 Years*.
- Brintjes, R., & Yates, D. . (2003). *Report on review and assessment of the potential for cloud seeding to enhance rain- fall in the Sultanate of Oman*. – NCAR, Boulder, Colorado, USA.

- Bruintjes, R. T. (1999). A Review of Cloud Seeding Experiments to Enhance Precipitation and Some New Prospects. *Bulletin of the American Meteorological Society*, 80(5), 805–820. [https://doi.org/10.1175/1520-0477\(1999\)080<0805:AROCSE>2.0.CO;2](https://doi.org/10.1175/1520-0477(1999)080<0805:AROCSE>2.0.CO;2)
- Chambers, R., Beare, S., Peak, S., & Al-Kalbani, M. (2016). Using ground-based ionisation to enhance rainfall in the Hajar Mountains, Oman. *Arabian Journal of Geosciences*, 9(7), 1–16. <https://doi.org/10.1007/s12517-016-2515-6>
- Chaouch, N., Temimi, M., Weston, M., & Ghedira, H. (2017). Sensitivity of the meteorological model WRF-ARW to planetary boundary layer schemes during fog conditions in a coastal arid region. *Atmospheric Research*, 187, 106–127. <https://doi.org/10.1016/j.atmosres.2016.12.009>
- Chowdhury, R., Mohamed, M. M. A., & Murad, A. (2016). ScienceDirect Variability of Extreme Hydro-Climatic Parameters in the North-Eastern Region of United Arab Emirates. *Procedia Engineering*, 154, 639–644. <https://doi.org/10.1016/j.proeng.2016.07.563>
- Corsmeier, U., Kalthoff, N., Barthlott, C., Aoshima, F., Behrendt, A., Di Girolamo, P., et al. (2011). Processes driving deep convection over complex terrain: a multi-scale analysis of observations from COPS IOP 9c. *Quarterly Journal of the Royal Meteorological Society*, 137(S1), 137–155. <https://doi.org/10.1002/qj.754>
- Eager, R. E., Raman, S., Wootten, A., Westphal, D. L., Reid, J. S., Al Mandoos, A., et al. (2008). A climatological study of the sea and land breezes in the Arabian Gulf region. *J. Geophys. Res.*, 113, 15106. <https://doi.org/10.1029/2007JD009710>
- Findell, K. L., & Eltahir, E. A. B. (2003). Atmospheric Controls on Soil Moisture–Boundary Layer Interactions. Part I: Framework Development. *Journal of Hydrometeorology*, 4(3), 552–569. [https://doi.org/10.1175/1525-7541\(2003\)004<0552:ACOSML>2.0.CO;2](https://doi.org/10.1175/1525-7541(2003)004<0552:ACOSML>2.0.CO;2)
- Fonseca, R., Temimi, M., Thota, M. S., Nelli, N. R., Weston, M. J., Suzuki, K., et al. (2020). On the Analysis of the Performance of WRF and NICAM in a Hyperarid Environment. *Weather and Forecasting*, 35(3), 891–919. <https://doi.org/10.1175/waf-d-19-0210.1>
- Francis, D., Temimi, M., Fonseca, R., Nelli, N. R., Abida, R., Weston, M., & Whebe, Y. (2020). On the Analysis of a Summertime Convective Event in a Hyperarid Environment. *Quarterly Journal of the Royal Meteorological Society*, qj.3930. <https://doi.org/10.1002/qj.3930>
- Görsdorf, U., Lehmann, V., Bauer-Pfundstein, M., Peters, G., Vavriv, D., Vinogradov, V., & Volkov, V. (2015). A 35-GHz polarimetric doppler radar for long-term observations of cloud parameters-description of system and data processing. *Journal of Atmospheric and Oceanic Technology*, 32(4), 675–690. <https://doi.org/10.1175/JTECH-D-14-00066.1>
- Groenemeijer, P., Barthlott, C., Behrendt, A., Corsmeier, U., Handwerker, J., Kohler, M., et al. (2009). Observations of kinematics and thermodynamic structure surrounding a convective storm cluster over a low mountain range. *Monthly Weather Review*, 137(2), 585–602. <https://doi.org/10.1175/2008MWR2562.1>
- Heinze, R., Dipankar, A., Henken, C. C., Moseley, C., Sourdeval, O., Trömel, S., et al. (2017). Large-eddy simulations over Germany using ICON: a comprehensive evaluation. *Quarterly Journal of the Royal Meteorological Society*, 143(702), 69–100. <https://doi.org/10.1002/qj.2947>
- Hersbach, H., Bell, B., Berrisford, P., Hirahara, S., Horányi, A., Muñoz-Sabater, J., et al. (2020). The ERA5 global reanalysis. *Quarterly Journal of the Royal Meteorological Society*, 146(730), 1999–2049. <https://doi.org/10.1002/qj.3803>

- Karagulian, F., Temimi, M., Ghebreyesus, D., Weston, M., Kondapalli, N. K., Valappil, V. K., et al. (2019). Analysis of a severe dust storm and its impact on air quality conditions using WRF-Chem modeling, satellite imagery, and ground observations. *Air Quality, Atmosphere and Health*, 12(4), 453–470. <https://doi.org/10.1007/s11869-019-00674-z>
- Kawabata, T., Schwitalla, T., Adachi, A., Bauer, H.-S., Wulfmeyer, V., Nagumo, N., & Yamauchi, H. (2018). Observational operators for dual polarimetric radars in variational data assimilation systems (PolRad VAR v1.0). *Geoscientific Model Development*, 11(6), 2493–2501. <https://doi.org/10.5194/gmd-11-2493-2018>
- Kumar, K. N., & Suzuki, K. (2019). Assessment of seasonal cloud properties in the United Arab Emirates and adjoining regions from geostationary satellite data. *Remote Sensing of Environment*, 228, 90–104. <https://doi.org/https://doi.org/10.1016/j.rse.2019.04.024>
- Lange, D., Behrendt, A., & Wulfmeyer, V. (2019). Compact Operational Tropospheric Water Vapor and Temperature Raman Lidar with Turbulence Resolution. *Geophysical Research Letters*, 46(24), 14844–14853. <https://doi.org/10.1029/2019GL085774>
- Macke, A., Seifert, P., Baars, H., Barthlott, C., Beekmans, C., Behrendt, A., et al. (2017). The HD(CP)2; Observational Prototype Experiment (HOPE) – an overview. *Atmospheric Chemistry and Physics*, 17(7), 4887–4914. <https://doi.org/10.5194/acp-17-4887-2017>
- NCAR (2005). *Rainfall enhancement and air chemistry studies: United Arab Emirates, Final Report on the Rainfall Enhancement Assessment Program in the UAE (2001–2005)*, 557 pp., Research Applications Program, National Center for Atmospheric Research, Boulder, Colorado. Accessed March 2018 at <http://www.gccmet.net/libraries/download/5>
- Nelli, N. R., Temimi, M., Fonseca, R. M., Weston, M. J., Thota, M. S., Valappil, V. K., Branch, O., Wulfmeyer, V., et al. (2020). Impact of Roughness Length on WRF Simulated Land-Atmosphere Interactions Over a Hyper-Arid Region. *Earth and Space Science*, 7(6). <https://doi.org/10.1029/2020ea001165>
- Nelli, N. R., Temimi, M., Fonseca, R. M., Weston, M. J., Thota, M. S., Valappil, V. K., Branch, O., Wizemann, H. D., et al. (2020). Micrometeorological measurements in an arid environment: Diurnal characteristics and surface energy balance closure. *Atmospheric Research*, 234, 104745. <https://doi.org/10.1016/j.atmosres.2019.104745>
- Odhiambo, G. O. (2017). Water scarcity in the Arabian Peninsula and socio-economic implications. *Applied Water Science*, 7(5), 2479–2492. <https://doi.org/10.1007/s13201-016-0440-1>
- Pal, J. S., & Eltahir, E. A. B. (2016). Future temperature in southwest Asia projected to exceed a threshold for human adaptability. *Nature Climate Change*, 6(2), 197–200. <https://doi.org/10.1038/nclimate2833>
- Pu, Z., Zhang, L., & Emmitt, G. D. (2010). Impact of airborne Doppler wind lidar profiles on numerical simulations of a tropical cyclone. *Geophysical Research Letters*, 37(5), n/a-n/a. <https://doi.org/10.1029/2009GL041765>
- Ranjha, R., Tjernström, M., Semedo, A., Svensson, G., & Cardoso, R. M. (2015). Structure and variability of the Oman coastal low-level jet. *Tellus, Series A: Dynamic Meteorology and Oceanography*, 67(1), 1–22. <https://doi.org/10.3402/tellusa.v67.25285>
- Schwitalla, T., & Wulfmeyer, V. (2014a). Radar data assimilation experiments using the IPM WRF Rapid Update Cycle. *Meteorologische Zeitschrift*, 23(1), 79–102. <https://doi.org/10.1127/0941-2948/2014/0513>

- Schwitalla, T., & Wulfmeyer, V. (2014b). Radar data assimilation experiments using the IPM WRF Rapid Update Cycle. *Meteorologische Zeitschrift*, 23(1), 79–102. <https://doi.org/10.1127/0941-2948/2014/0513>
- Schwitalla, T., Branch, O., & Wulfmeyer, V. (2020). Sensitivity study of the planetary boundary layer and microphysical schemes to the initialization of convection over the Arabian Peninsula. *Quarterly Journal of the Royal Meteorological Society*, 146(727), 846–869. <https://doi.org/10.1002/qj.3711>
- Sherif, M., Almulla, M., Shetty, A., & Chowdhury, R. K. (2014). Analysis of rainfall, PMP and drought in the United Arab Emirates. *International Journal of Climatology*, 34(4), 1318–1328. <https://doi.org/10.1002/joc.3768>
- Smith, V. H., Mobbs, S. D., Burton, R. R., Hobby, M., Aoshima, F., Wulfmeyer, V., & Di Girolamo, P. (2014). The role of orography in the regeneration of convection: A case study from the convective and orographically-induced precipitation study. *Meteorologische Zeitschrift*, 24(1), 83–97. <https://doi.org/10.1127/metz/2014/0418>
- Späth, F., Behrendt, A., Kumar Muppa, S., Metzendorf, S., Riede, A., & Wulfmeyer, V. (2016). 3-D water vapor field in the atmospheric boundary layer observed with scanning differential absorption lidar. *Atmospheric Measurement Techniques*, 9(4), 1701–1720. <https://doi.org/10.5194/amt-9-1701-2016>
- Steinhoff, D. F., Brientjes, R., Hackera, J., Keller, T., Williams, C., Jensen, T., et al. (2018). Influences of the monsoon trough and Arabian heat low on summer rainfall over the United Arab Emirates. *Monthly Weather Review*, 146(5), 1383–1403. <https://doi.org/10.1175/MWR-D-17-0296.1>
- Temimi, M., Fonseca, R. M., Nelli, N. R., Valappil, V. K., Weston, M. J., Thota, M. S., et al. (2020). On the analysis of ground-based microwave radiometer data during fog conditions. *Atmospheric Research*, 231, 104652. <https://doi.org/10.1016/j.atmosres.2019.104652>
- Thundathil, R., Schwitalla, T., Behrendt, A., Muppa, S. K., Adam, S., & Wulfmeyer, V. (2020). Assimilation of Lidar Water Vapour Mixing Ratio and Temperature Profiles into a Convection-Permitting Model. *Journal of the Meteorological Society of Japan. Ser. II*, 98(5), 959–986. <https://doi.org/10.2151/jmsj.2020-049>
- Valappil, V. K., Temimi, M., Weston, M., Fonseca, R., Nelli, N. R., Thota, M., & Kumar, K. N. (2020). Assessing Bias Correction Methods in Support of Operational Weather Forecast in Arid Environment. *Asia-Pacific Journal of Atmospheric Sciences*, 56(3), 333–347. <https://doi.org/10.1007/s13143-019-00139-4>
- Weckwerth, T. M., Wilson, J. W., Wakimoto, R. M., & Crook, N. A. (1997). Horizontal Convective Rolls: Determining the Environmental Conditions Supporting their Existence and Characteristics. *Monthly Weather Review*, 125(4), 505–526. [https://doi.org/10.1175/1520-0493\(1997\)125<0505:HCRDTE>2.0.CO;2](https://doi.org/10.1175/1520-0493(1997)125<0505:HCRDTE>2.0.CO;2)
- Wehbe, Y., Temimi, M., Weston, M., Chaouch, N., Branch, O., Schwitalla, T., et al. (2019). Analysis of an extreme weather event in a hyper-arid region using WRF-Hydro coupling, station, and satellite data. *Natural Hazards and Earth System Sciences*, 19(6), 1129–1149. <https://doi.org/10.5194/nhess-19-1129-2019>
- Wehbe, Y., Temimi, M., & Adler, R. F. (2020). Enhancing precipitation estimates through the fusion of weather radar, satellite retrievals, and surface parameters. *Remote Sensing*, 12(8), 1342. <https://doi.org/10.3390/RS12081342>

- Weston, M., Chaouch, N., Valappil, V., Temimi, M., Ek, M., & Zheng, W. (2019). Assessment of the Sensitivity to the Thermal Roughness Length in Noah and Noah-MP Land Surface Model Using WRF in an Arid Region. *Pure and Applied Geophysics*, 176(5), 2121–2137. <https://doi.org/10.1007/s00024-018-1901-2>
- Wulfmeyer, V., Behrendt, A., Kottmeier, C., Corsmeier, U., Barthlott, C., Craig, G. C., et al. (2011). The Convective and Orographically-induced Precipitation Study (COPS): The scientific strategy, the field phase, and research highlights. *Quarterly Journal of the Royal Meteorological Society*, 137(SUPPL. 1), 3–30. <https://doi.org/10.1002/qj.752>
- Wulfmeyer, V., Branch, O., Warrach-Sagi, K., Bauer, H. S., Schwitalla, T., & Becker, K. (2014). The impact of plantations on weather and climate in coastal desert regions. *Journal of Applied Meteorology and Climatology*, 53(5), 1143–1169. <https://doi.org/10.1175/JAMC-D-13-0208.1>
- Wulfmeyer, V., Hardesty, R. M., Turner, D. D., Behrendt, A., Cadeddu, M. P., Di Girolamo, P., et al. (2015, September 1). A review of the remote sensing of lower tropospheric thermodynamic profiles and its indispensable role for the understanding and the simulation of water and energy cycles. *Reviews of Geophysics*. Blackwell Publishing Ltd. <https://doi.org/10.1002/2014RG000476>
- Yousef, L. A., Temimi, M., Wehbe, Y., & Al Mandous, A. (2019). Total cloud cover climatology over the United Arab Emirates. *Atmospheric Science Letters*, 20(2), e883. <https://doi.org/10.1002/asl.883>

## Appendix

**Table A1: Specification and operation details of DL and DCR.**

Streamline XR Doppler lidar	
Specifications	
Manufacturer	HALO Photonics
Type	Moveable scanner, all hemispherical directions
Wavelength	1.5 $\mu\text{m}$
Pulse repetition	10 kHz
Stated line-of-sight range	12 km
Variables	Line-of-sight Doppler velocity, backscatter coefficient, signal-to-noise ratio
RHI scans	190° vertical scans from -5° to 185° elevation angles at 0°, 30°, 60°, 90°, 120°, and 150° azimuth angles
PPI scans	360° azimuthal scans at 0° and 45° elevation angles
Scan synchronicity	All RHIs and PPIs synchronized with their equivalents in the DCR
Scan speed, integration time, angular resolution	3°/s, 1 s, and 3° respectively

Range resolution	60 m
Scan sequence duration	15 mins
Measurement period	Jul 2017-Apr 2019
Data availability	>70%
Significant breaks	31 August 2017 to 1 February 2018 – sensor maintenance
Quicklooks	Available at <a href="https://ocal.uni-hohenheim.de/en/rc1">https://ocal.uni-hohenheim.de/en/rc1</a>
<b>MIRA-35 Doppler cloud radar</b>	
Specifications	
Manufacturer	Metek GmbH
Type	Moveable scanner, all hemispherical directions
Frequency	Ka-band, 35.1 GHz
Peak power	30 kW
Pulse length	200 ns
Pulse repetition frequency	5 kHz
Minimum range	0.15 km
Maximum range	15 km
Range resolution	30 m
No. of pulses for FFT	256
No. of spectra for averaging	200
Sensitivity at 5 km	-55 dBZ
Variables	Line-of-sight Doppler velocity, radar reflectivity, peak width, linear depolarization ratio and skewness
RHI scans	180° vertical scans from 0° to 180° elevation angles at 0°, 30°, 60°, 90°, 120°, and 150° azimuth angles
PPI scans	360° azimuthal scans at 5° and 45° elevation angles
Scan synchronicity	Synchronized with DL
Scan speed, integration time, angular resolution	3°/s, 1 s, and 3° respectively
Range resolution	30m
Scan sequence duration	15 min
Measurement period	Jul 2017-Apr 2019
Data availability	>95%



Significant breaks	3 October 2018 to 31 October 2018 - DCR scanner cable maintenance
Quicklooks	Available at <a href="https://ocal.uni-hohenheim.de/en/rc1">https://ocal.uni-hohenheim.de/en/rc1</a>

## **Acknowledgments, Samples, and Data**

The authors of this paper have no real or perceived financial conflicts of interests in carrying out this work.

This material is based on work supported by the UAE Research Program for Rain Enhancement Science, under the National Center of Meteorology, Abu Dhabi, UAE.

Special thanks to all other colleagues at the Masdar Institute (now Khalifa University), the National Center for Meteorology, and the UAEREP for their scientific and logistical support in the realization of this project.

Data availability – All DL and DCR raw data for 5 and 6 September is available at <https://zenodo.org/record/4287382>. The DL and DCR imagery, and ECMWF, precipitation radar and sounding data for 5 and 6 September 2018 is available for download at: <https://doi.org/10.5281/zenodo.4267815>. Quicklook data for the 19 month measurement period is available to browse and download on the Metek GmbH server, accessible at <https://ocal.uni-hohenheim.de/en/rc1>.